DEEP SEQUENCING OF SOMATOSENSORY NEURONS REVEALS MOLECULAR DETERMINANTS OF INTRINSIC PHYSIOLOGICAL PROPERTIES

by

Yang Zheng

A dissertation submitted to Johns Hopkins University in conformity with the requirements for the degree of Doctor of Philosophy

Baltimore, Maryland

November, 2018

ABSTRACT

Dorsal root ganglion (DRG) sensory neuron subtypes defined by their *in vivo* properties display distinct intrinsic electrical properties. Here we used deep RNA-sequencing of genetically-labeled neurons and electrophysiological analyses to define ion channel contributions to the intrinsic electrical properties of DRG sensory neuron subtypes. The transcriptome profiles of eight DRG neuron subtypes revealed a large set of differentially expressed and functionally relevant genes, including voltage-gated ion channels. Guided by these data, electrophysiological analyses using pharmacological and genetic manipulations of sensory neuron subtypes were undertaken to assess the functions of select voltage-gated potassium channels in shaping action potential (AP) waveforms and firing patterns. Our findings indicate that the transcriptome profiles are highly predictive of ion channel contributions to sensory neuron subtype-specific intrinsic physiological properties. The distinct ensembles of voltage-gated ion channels predicted to underlie the unique intrinsic physiological properties of eight major DRG neuron subtypes are presented.

Thesis Advisor and Reader #1	David Ginty, Ph.D.
Committee Chair	King-Wai Yau, Ph.D.
Committee Member and Reader #2	Bruce Bean, Ph.D.
Committee Member	David Corey, Ph.D.
Committee Member	Stephen Liberles, Ph.D.

ACKNOWLEDGEMENT

This work is only possible with collaboration, help and guidance from many others. Here, I'd like to acknowledge all the people who were directly involved in the research project and the people who inspired and supported me along this journey.

First, I would like to thank my advisor, Dr. David Ginty for his tremendous amount of guidance and support and the resources he provided for this project, as well as his mentorship. David's ingenious intuition in science, creativity and critical thinking constantly educated me and tremendously influenced how I identify key questions in science, approach these questions experimentally, interpret results and identify potential pitfalls. David has also educated me how to deliver research and ideas in the form of presentations and paper, as well as short conversations. He supported me in developing new skills and exploring ideas, which greatly helped me mature as a scientist. Moreover, David genuinely cared about the well-being of lab members. Beyond being a great mentor, David truly demonstrated the spirit of being a great scientist, dedicated, enthusiastic and hardworking.

Many people contributed to or helped with the research presented here. In particular, Dr. Pin Liu and Dr. Bruce Bean at Harvard Medical School served as core collaborators and their contributions elevated and transformed this project. Pin did all the voltage and current clamp electrophysiology experiments, which constitutes a key part of this research project. The experiments with Aβ neuron subtypes were only made possible by

Pin, the grandmaster of *in vitro* patch-clamp, and her exquisite skills. Bruce brought his encyclopedic knowledge of ion channels to this project and was the mastermind behind selecting channel targets to test. Bruce also served as my second mentor and offered great help and advice. There were many occasions when I just showed up at Bruce's office with loads of questions, and never even once I came back without answers. Bruce's pure passion and dedication for ion channel research motivated me as a scientist. I thank Bruce and Pin also for bringing in a fresh angle to this project, for generating the many idea-stimulating meetings, and for all the pleasure I had working together.

I'd also like to thank Dr. Ling Bai for her help with purification and RNA-sequencing of Aδ-LTMRs and Aβ Field-LTMRs as well as her mentorship during my rotation in the Ginty lab. I'd like to thank Dr. James Trimmer for Kv4.3 antibody and advice in immunostaining; Dr. Ting Guo for his advice during the early stages of this project; Dr. Hao Zhang at the Johns Hopkins Bloomberg Flow Cytometry and Immunology Core for his help with FACS, which greatly facilitated the process; Dr. Haiping Hao, Jasmeet Sethi and Linda Orzolek at the Johns Hopkins Deep Sequencing & Microarray Core Facility for help with RNA-sequencing; Dr. Meeta Mistry at the Harvard School of Public Health Bioinformatics Core for help with Bioinformatics, Sarah Bahai from Simmons College for help with mouse husbandry and histological experiments; and Gui-Lan Yao for help with histological experiments.

My sincere thanks go to my thesis committee members, Dr. Bruce Bean, Dr. David Corey, Dr. Stephen Liberles and Dr. King-Wai Yau for their insightful feedbacks and their effort reading my dissertation.

I also thank all current and former Ginty lab members for all the discussions and feedbacks on this project and for creating a friendly, engaging, idea-stimulating environment. Special thanks go to members who developed mouse genetic tools for specific labeling of different DRG neuron subtypes, which is the foundation of this study.

On a personal note, I thank my friends and family for their support. I thank my close friends Dr. Nicole Neubarth and Dr. Brendan Lehnert for inspiring me not only scientifically but also in many aspects of life. I am grateful to them for making my graduate school years a lot more enjoyable.

I thank my boyfriend Thomas for supporting me through difficult times, for making me happier every day and for constantly inspiring me to become a better person.

Last, I thank my parents, 阮晓梅 and 郑小鸣, for their unconditional love and endless support. I dedicate this thesis work to them.

TABLE OF CONTENTS

LIST OF TABLES

LIST OF FIGURES

CHAPTER 1. INTRODUCTION

Dorsal root ganglia (DRG) neurons are the first-order neurons in the somatosensory afferent pathway, transducing physical, thermal and chemical stimuli acting in the periphery into electrical signals conveyed to the spinal cord and brain for action and perception. DRG neurons are pseudo-unipolar, with one axonal branch that innervates peripheral tissues, including the skin, and another that projects to the spinal cord and, in some cases, the dorsal column nuclei of the brainstem (Abraira and Ginty, 2013). Decades of research has shown that DRG sensory neurons exhibit a diverse range of peripheral ending morphologies, central projection patterns, and physiological properties, and that they are tuned to distinct modalities or features of sensory stimuli. DRG neurons are thus classified into distinct subtypes (Abraira and Ginty, 2013; Basbaum et al., 2009; Delmas et al., 2011; Willis and Coggeshall, 2004; Woolf and Ma, 2007; Zimmerman et al., 2014).

How do DRG neuron subtypes transduce sensory stimuli into patterns of APs that propagate to the central nervous system? Stimuli impinging on the skin and other organs activate transduction receptors or ion channels on peripheral terminals of DRG sensory neurons, resulting in the generation of receptor potentials. Transduction channels include thermosensitive and mechanosensitive cation channels, such as TrpV1, TrpM8 and Piezo2 (Julius, 2013; Ranade et al., 2015). Receptor potentials generated at axon terminals may be integrated over space and time and subject to modulation by locally expressed voltage-gated ion channels (Bai et al., 2015; François et al., 2015; Grigg, 1986; Heidenreich et al., 2012; Wang and Lewin, 2011). Suprathreshold receptor potentials

trigger activation of voltage-gated ion channels at initiation sites to generate APs that propagate along the length of the axon, into its central axonal branches and terminals. AP thresholds and spike patterns are influenced by the biophysical properties and densities of voltage-gated ion channels located at the initiation site (Barkai et al., 2017; Grigg, 1986). The particular combination of voltage-gated ion channels present in a given neuron also determines the refractory period, maximum AP firing frequency, and successful propagation at the T-junction near the ganglion (Du et al., 2014; Sundt et al., 2015), as well as the magnitude and timing of neurotransmitter release at central synapses. Thus, while the transduction machinery determines the general stimulus modality to which DRG sensory neurons respond, voltage-gated ion channels modulate generator currents and control AP thresholds, AP firing patterns, propagation, and synaptic transmission, and are therefore critical determinants of DRG sensory neuron function.

It has long been established that a wide range of voltage-gated sodium (Nav), calcium (Cav), and potassium (Kv) channels are expressed in DRG neurons, and several of these ion channels are now appreciated as targets for developing drugs to treat pain (Dib-Hajj et al., 2010; Tsantoulas and McMahon, 2014; Waxman and Zamponi, 2014). Most electrophysiological studies have focused on small-diameter DRG neurons, most (but not all) of which correspond to unmyelinated nociceptors, with some studies distinguishing sub-populations of small-diameter neurons based on lectin binding or capsaicin sensitivity (Du and Gamper, 2013; Petruska et al., 2000; Rau et al., 2014; Vydyanathan et al., 2005). Much less is known about the complement of ion channels in physiologically-defined DRG neuron subtypes (for example, mechanoreceptors) or how they relate to the

firing behaviors in these subtypes, especially medium- and large-diameter DRG neurons, which comprise a highly heterogenous population. Therefore, a major current challenge is determining how intrinsic electrical properties of the diverse, physiologically distinct mammalian somatosensory neuron subtypes are specified to shape their unique sensitivities, firing patterns, transmitter release properties, and functions.

Recent advances in the development of mouse genetic tools to interrogate the major classes of DRG sensory neurons afford an opportunity to investigate the relationship between patterns of voltage-gated ion channel expression and the intrinsic physiological properties of DRG neuron subtypes. Genetic tools now exist for labeling five principal low-threshold mechanoreceptor (LTMRs, i.e., touch receptors) subtypes that innervate the hairy skin: these are the C-LTMRs, Aδ-LTMRs, Aβ RA-LTMRs, Aβ SA1-LTMRs, and Aβ Field-LTMRs (Zimmerman et al., 2014). Here, we used genetic tools to identify intrinsic molecular determinants of the physiological properties of LTMR subtypes and, for comparison, nociceptor subtypes and proprioceptors (Hippenmeyer et al., 2005; Zylka et al., 2005). We employed genetic labeling to purify these DRG neuron subtypes and performed deep RNA-sequencing to identify candidate genes that underlie their subtype-specific intrinsic electrophysiological properties. Our analysis revealed many genes, including voltage-gated ion channels, that are differentially expressed across the five LTMR subtypes, peptidergic and polymodal nonpeptidergic nociceptors, and proprioceptors. Guided by these gene expression profiles, we performed electrophysiological experiments to define contributions of differentially expressed Kv channels to sensory neuron subtype-specific intrinsic electrical properties. Our findings

support a predictive model of the distinct voltage-gated ion channel constellations that support the unique intrinsic properties of the major DRG sensory neuron classes.

CHAPTER 2. EXPERIMENTAL RESULTS

Subtype-Specific Intrinsic Electrical Properties and Mechanosensitivity of DRG Neurons

While prior studies have used *in vitro* electrophysiological recordings to reveal a wide range of intrinsic membrane properties of DRG neurons, these analyses mainly examined the properties of neurons defined by cell size, TRP channel expression, or isolectin B4 (IB4) binding, rather than *in vivo* functional profiles. The availability of mouse genetic tools for selective labeling of functionally defined sensory neuron subtypes *in vivo* now enables a near comprehensive analysis of subtype-specific intrinsic physiological properties of these subtypes. We focused on eight major classes of DRG sensory neurons labeled *in vivo* using genetically modified mice. These are the $MrgD^{+}$ polymodal nonpeptidergic nociceptors, the broad class of $CGRP^{+}$ peptidergic nociceptors, five functionally defined LTMR subtypes (C-LTMRs, Aδ-LTMRs, Aβ RA-LTMRs, Aβ SA1-LTMRs, Aβ Field-LTMRs), and proprioceptors. The genetic tools used to label each of these neuronal populations are as in Table 2.1.1: $MrgD^{EGFP}$ mice to label $MrgD^{+}$ polymodal nociceptors (Zylka et al., 2005), Calca (CGRP)-EGFP BAC transgenic mice for peptidergic nociceptors (Bai et al., 2015), $Th^{2A\text{-}CreER}$; $R26^{lsl\text{-}tdTomato}$ *(Ai14)* mice

---

The work described in this chapter represents a collaboration between Yang Zheng and Dr. Pin Liu. Dr. Pin Liu performed the *in vitro* voltage and current clamp electrophysiological experiments using genetically labeled or modified mice generated by Yang Zheng.

(Tamoxifen 2 mg/day at P13-14) for C-LTMRs (Abraira et al., 2017), *TrkB^{CreER}; Ai14* mice (Tamoxifen 2 mg/day at E12.5-13.5) and *TrkB^{tauEGFP}* for Aδ-LTMRs (Rutlin et al., 2014), Npy2r-GFP BAC transgenic mice for Aβ RA-LTMRs (Li et al., 2011); *Trk^{CreER}; Ret^{fGFP}* mice (Tamoxifen 3mg at E12.5) for Aβ SA1-LTMRs; *TrkC^{CreER}; Ret^{fGFP}* mice (Tamoxifen 2 mg/day at P13.5-14.5) for Aβ Field-LTMRs (Bai et al., 2015), and *PV$^{IRES-Cre}$; Ai14* mice to label proprioceptors (Hippenmeyer et al., 2005). We estimate that these eight populations account for ~85% of all DRG neurons (Bai et al., 2015; Gorokhova et al., 2014; Li et al., 2011; Lu et al., 2017).

2.1. Somatosensory neurons exhibit subtype-specific intrinsic electrical properties

To define the intrinsic electrical properties of DRG neuron subtypes, neurons from each of the genetically labeled mouse lines were acutely dissociated and used for *in vitro* whole-cell patch-clamp recordings. Overall, most subtypes displayed distinct electrophysiological signatures, although two subtypes, Aβ Field-LTMRs and Aβ SA1-LTMRs, were largely indistinguishable. In response to sustained current injections of increasing amplitude, MrgD^{+} nonpeptidergic nociceptors and C-LTMRs both showed repetitive low-frequency firing, reaching maximum frequencies of about 12 Hz and 26 Hz, respectively (Figure 2.1.1 A, B and H). C-LTMRs exhibited an unusual firing pattern with a long delay to the first AP followed by regular repetitive spiking (Figure 2.1.1 B). Aδ-LTMRs showed strong adaptation, firing 5-6 spikes in the first few hundred ms and then becoming silent (Figure 2.1.1 C and H). Aβ RA-LTMRs and proprioceptors both fired repetitively over a wide range of frequencies, with the frequency increasing with current amplitude, to a maximum of ~180 and ~220 Hz, respectively (Figure 2.1.1 D, G

and H). Both Aβ Field-LTMRs and Aβ SA1-LTMRs typically displayed very strong adaptation, firing only in the first 50 ms of current injection (Figure 2.1.1 E, F and H). Strikingly, Aβ SA1-LTMRs fired no more than two spikes regardless of the current intensity used for stimulation.

The finding that Aβ SA1-LTMRs fire non-repetitively to sustained current injection *in vitro* is counterintuitive since these neurons fire repetitively and adapt slowly to sustained skin indentation *in vivo* (Woo et al., 2015; Zimmerman et al., 2014). We therefore asked whether Aβ SA1-LTMRs could fire repetitively *in vitro* by applying a train of short current pulses (250 μs). Indeed, all Aβ SA1-LTMRs tested faithfully followed pulse stimulation up to ~300Hz (Figure 2.1.1 I). *In vivo*, Aβ SA1-LTMR cutaneous endings are associated with Merkel cells, which are themselves mechanosensitive and transmit excitatory signals to Aβ SA1-LTMRs (Ikeda et al., 2014; Maksimovic et al., 2014; Wellnitz et al., 2010). These in vitro results are thus consistent with the notion that the repetitive firing of Aβ SA1-LTMRs in response to static indentation in vivo depends on their association with Merkel cells (Nakatani et al., 2014; Woo et al., 2015). Proprioceptors could follow repetitive stimulation at even higher frequencies (400-600 Hz) than Aβ SA1-LTMRs and maximal firing frequencies of both were far higher than that achieved by C-LTMRs (30-100 Hz).

The DRG neuron subtypes were also distinguished by their AP waveforms. $MrgD^{+}$ nonpeptidergic nociceptors and C-LTMRs have much wider APs (widths ~2 ms at half spike height), compared to those measured in other LTMR subtypes and proprioceptors,

which have widths shorter than 0.5 ms (Figure 2.1.2). The broad APs seen in MrgD$^+$ nonpeptidergic nociceptors and C-LTMRs agree with previous results showing broad APs in cell bodies associated with unmyelinated C-fibers in rats (Harper and Lawson, 1985). Broad APs may help facilitate effective AP propagation in small unmyelinated axons with correspondingly short length constants, which are susceptible to spike failure, especially at the T-junction of the dorsal root ganglion (Gemes et al., 2013; Sundt et al., 2015).

Our electrophysiological analyses of MrgD$^+$ nonpeptidergic nociceptors, the five LTMR subtypes, and proprioceptors indicate that these populations are largely homogeneous in terms of within-group firing patterns and AP waveforms. On the other hand, the CGRP$^+$ peptidergic nociceptors displayed a range of firing patterns and AP waveforms (Figure 2.1.3), consistent with the idea that CGRP labels a large, functionally and morphologically heterogeneous group of neurons that can be further subdivided based on their intrinsic physiological properties (Arcourt et al., 2017; Bardoni et al., 2014; Han et al., 2013; Patil et al., 2018).

Table 2.1.1. Genetic toolbox for labeling eight DRG sensory neuron subtypes.

Neuronal Subtypes	Labeling Strategy
Nonpeptidergic Nociceptors	*MrgD*^{EGFP}
Peptidergic Nociceptors	CGRPα-EGFP
C-LTMRs	*TH*$^{2A\text{-}CreER}$;*R26*$^{LSL\text{-}tdTomato}$ TAM@P13.5-14.5
Aδ-LTMRs	*TrkB*^{CreER};*R26*$^{LSL\text{-}tdTomato}$ TAM@E12.5-14.5 (1)
	TrkB^{tauEGFP} (2)
Aβ RA-LTMRs	Npy2r-GFP
Aβ SA1-LTMRs	*TrkC*^{CreER};*Ret*^{tGFP} TAM@E12.5
Aβ Field-LTMRs	*TrkC*^{CreER};*Ret*^{tGFP} TAM@P12.5-14.5
Proprioceptors	*PV*$^{iresCre;}$*R26*$^{LSL\text{-}tdTomato}$

(1) was used in RNA-sequencing and electrophysiology experiments of whole-cell current and voltage clamp.

(2) was used only for mechanoclamp experiment, related to Figure 2.2.1.

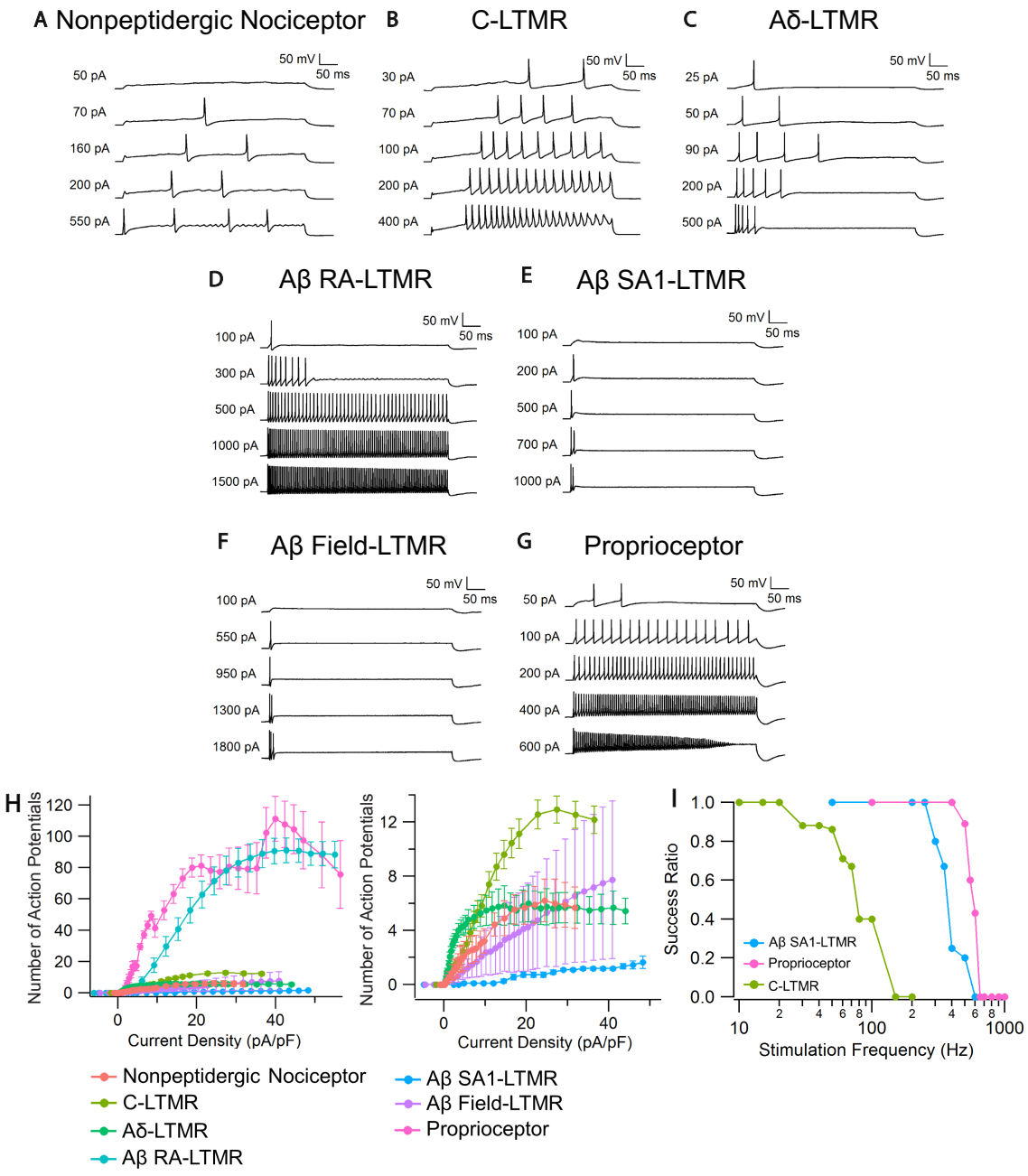

Figure 2.1.1. Distinct spiking patterns of seven DRG sensory neuron subtypes.

(**A-G**) Representative *in vitro* spiking patterns of DRG neuron subtypes during 500-ms injection of depolarizing current steps of increasing magnitude. Current magnitudes are reported in pA.

(**H**) Number of APs during 500-ms current injections for each subtype shown in (**A-G**) plotted against current density. An enlarged image for neuronal subtypes that have lower spike numbers is shown in the right panel. Group data are represented as mean ± standard error (SEM). APs satisfy the criteria that peak voltage is above -12 mV and spike height is at least 40mV. n=9 for $MrgD^{+}$ nonpeptidergic nociceptors; n=28 for C-LTMRs; n=19 for Aδ-LTMRs; n=25 for Aβ RA-LTMRs; n=11 for Aβ SA1-LTMRs; n=16 Aβ Field-LTMRs; n=14 for proprioceptors.

(**I**) Survival plot depicting the percentages of C-LTMRs (n=8), Aβ SA1-LTMRs (n=5) and proprioceptors (n=9) whose repetitive firing successfully followed 250 μs pulse stimulation at the indicated frequencies.

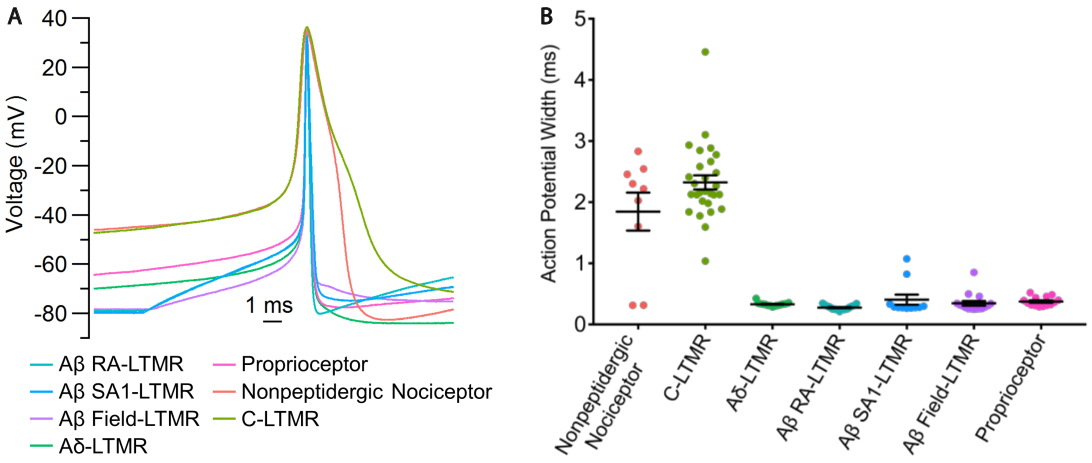

Figure 2.1.2. AP waveforms and widths of seven DRG sensory neuron subtypes.

(**A**) Representative AP waveforms of DRG neuron subtypes. The waveform shown is of the first AP evoked by injection of current as in Figure 2.1.1 (**A**-**G**) at or just above threshold.

(**B**) AP widths of DRG neuron subtypes. Group mean and SEM are shown (n as in Figure 2.1.1). The width is measured at half-maximal spike amplitude. Each data point was acquired by averaging the widths of the first AP evoked at all current magnitudes for one neuron. One-way ANOVA with Tukey's multiple comparisons test was used to show that MrgD^{+} nonpeptidergic nociceptors and C-LTMRs are different from each other ($p=0.036$) and from all other subtypes ($p<0.001$).

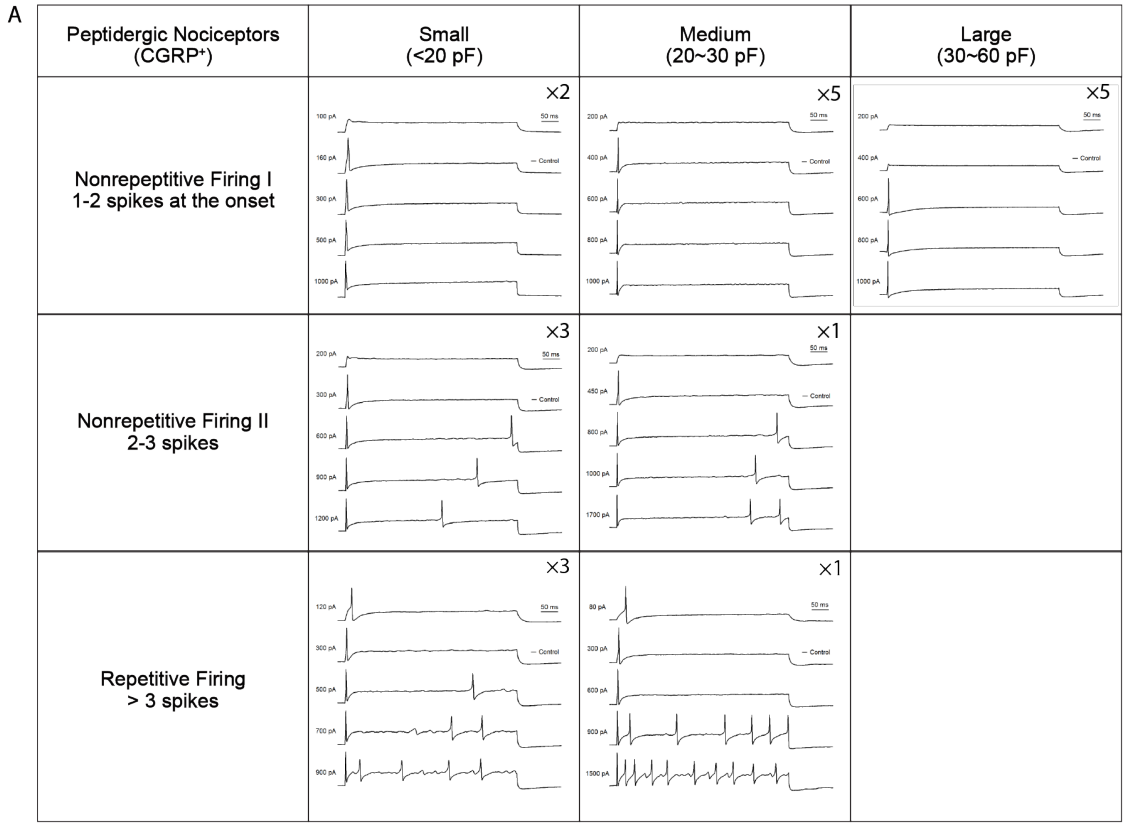

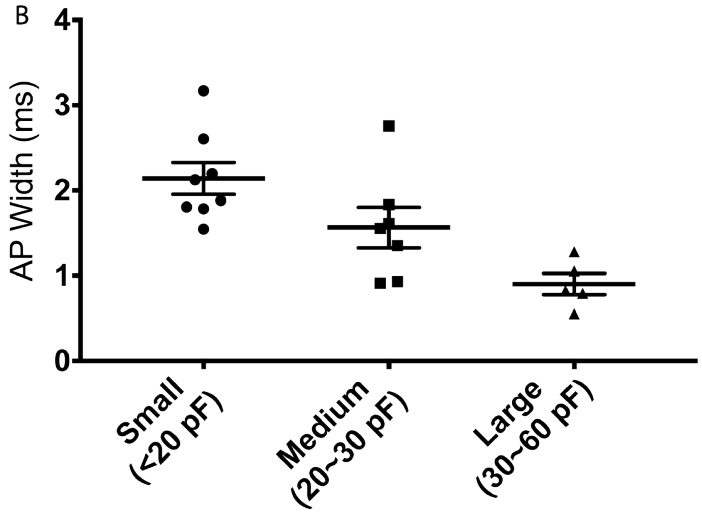

Figure 2.1.3. Heterogeneity of intrinsic electrical properties of peptidergic nociceptors.

(**A**) Representative *in vitro* spiking patterns of $CGRP^+$ peptidergic nociceptors during 500-ms injection of depolarizing current steps of increasing magnitude. Current step magnitudes are reported in pA. $CGRP^+$ peptidergic nociceptors are first categorized based on membrane capacitance, then by spiking patterns as indicated in the table. The number of neurons classified in each category is noted on the top-right corner of each cell.

(**B**) AP widths of $CGRP^+$ peptidergic nociceptors categorized based on membrane capacitance as in (**A**) (total n =20). The AP widths of the three subclasses of $CGRP^+$ peptidergic nociceptors are different. p=0.001, one-way ANOVA test.

2.2. DRG somatosensory neuron subtypes exhibit different mechanosensitive properties

To assess intrinsic mechanosensitivity of the DRG sensory neuron subtypes, genetically labeled DRG neurons were used for *in vitro* whole-cell mechanoclamp experiments in which a controlled mechanical stimulus was applied to the cell body using a piezo-driven glass probe and resulting currents were recorded (Hao and Delmas, 2011; McCarter et al., 1999). All labeled neuronal types were used for this analysis, except for $CGRP^+$ peptidergic nociceptors which were excluded because of their heterogeneous firing properties (Figure 2.1.3) (Patil et al., 2018). With a series of 500-ms mechanical stimulations of increasing displacement, all five LTMR subtypes and proprioceptors displayed obvious mechanically-activated inward currents (I_{mech}) (I_{mech} in five LTMRs and proprioceptors are significantly different from noise level (>100 pA)) (Figure 2.2.1 B-H), while the majority of $MrgD^+$ nonpeptidergic nociceptors displayed minimal or undetectable I_{mech} (majority of I_{mech} in $MrgD^+$ nonpeptidergic nociceptors <100 pA, and not significantly different from noise) (Figure 2.2.1 A and H). I_{mech} in DRG neuron subtypes also displayed different decay kinetics. I_{mech} of Aδ-LTMRs, Aβ-LTMRs, and proprioceptors have fast relaxation kinetics with a time constant (τ) mostly shorter than 30 ms (Figure 2.2.1 I). In comparison, I_{mech} of C-LTMRs decays slower with an average time constant around 100ms. Since one or two-component exponential fitting was used and fast τ was chosen to be plotted here, the slower current relaxation τ in C-LTMRs suggest a lack of fast adapting mechanotransducer. It is worth noting here, that the maximum amplitudes of I_{mech} are amplitudes of largest I_{mech} we ever recorded in each neuron, and did not saturate in most of the neurons (Figure 2.2.2) (Also See Experimental

Procedures). The differences of maximum amplitudes of I_{mech} among neuronal subtypes could be due to many potential factors other than intrinsic molecular machinery, such as the possibility of recruiting more mechanotransducers with larger displacement, thus, rendering further interpretation of the differences of the maximum amplitudes of I_{mech} across subtypes difficult.

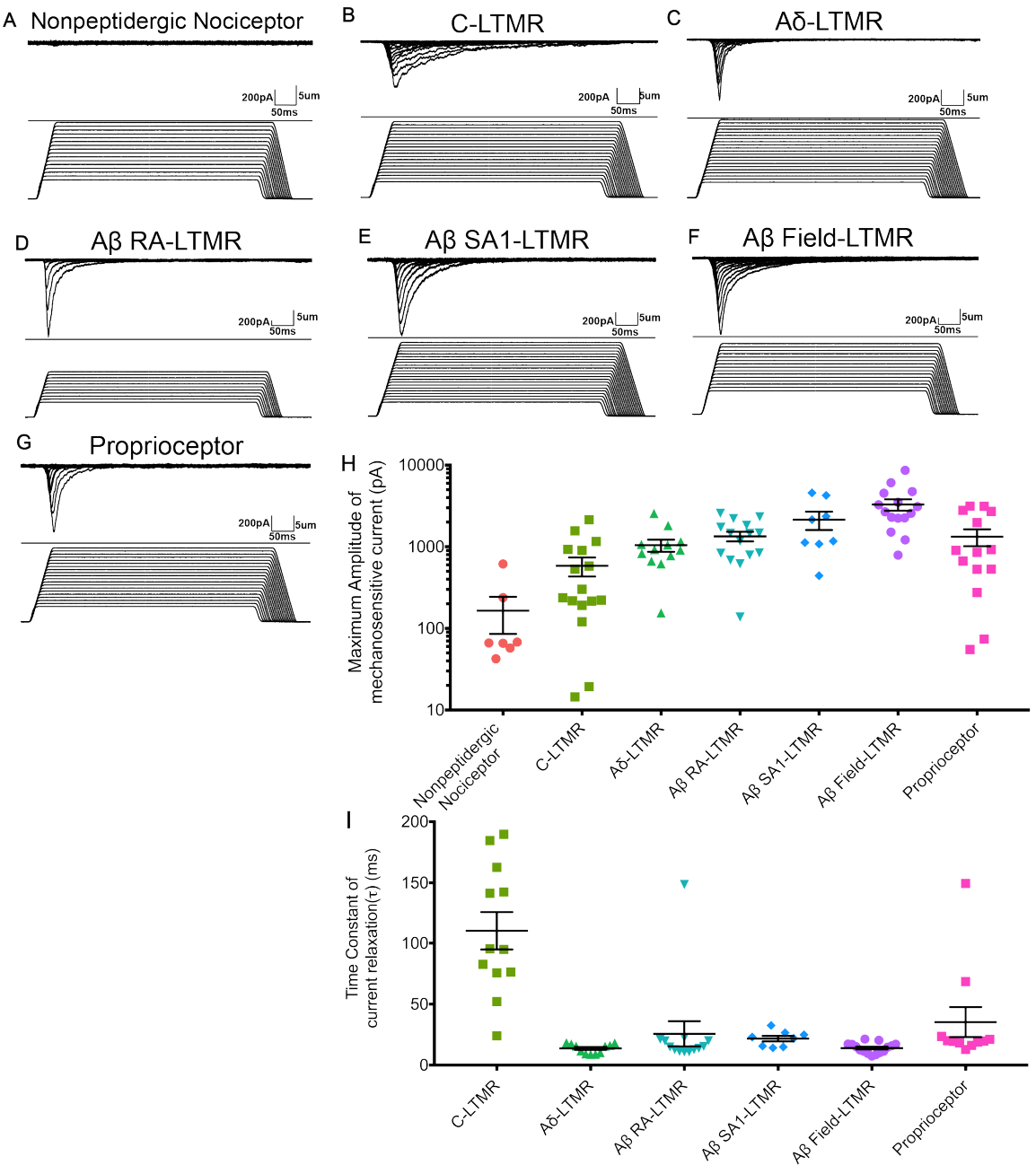

Figure 2.2.1. Distinct mechanosensitivity of seven major DRG sensory neuron subtypes.

(**A-G**) Representative traces of mechanically activated inward current during 500-ms step displacements of increasing magnitudes for each DRG neuron subtype.

(**H**) Maximal amplitudes of I_{mech} for each DRG neuron subtype. Values are the maximal amplitudes recorded. Group means and SEM are plotted. The maximal amplitudes of I_{mech} are significantly different ($p < 0.0001$). In particular, maximal amplitudes of I_{mech} measured in $MrgD^+$ nonpeptidergic nociceptors are significantly smaller than those measured in Aβ RA-LTMRs ($p = 0.0072$), Aβ SA1-LTMRs ($p = 0.0014$), Aβ Field-LTMRs ($p < 0.0001$) and proprioceptors ($p = 0.0345$). Kruskal-Wallis test with multiple comparisons of every subtype against $MrgD^+$ nonpeptidergic nociceptors. I_{mech} measured in $MrgD^+$ nonpeptidergic nociceptors is not significantly different from 100pA, which is the noise level ($p = 0.4450$), while I_{mech} measured in five LTMRs and proprioceptors are ($p < 0.01$). One-sample t-test. n = 7 for $MrgD^+$ nonpeptidergic nociceptors, n = 16 for C-LTMRs, n = 12 for Aδ-LTMRs; n = 15 for Aβ RA-LTMRs; n = 8 for Aβ SA1-LTMRs; n = 15 for Aβ Field-LTMRs and n = 14 for proprioceptors.

(**I**) Time constant (τ) of I_{mech} relaxation kinetics for each DRG neuron subtype. Group mean and SEM are shown using error bars. τ of I_{mech} are significantly different among subtypes ($p < 0.0001$). In particular, τ in C-LTMRs are significantly larger than those in Aδ-LTMRs ($p < 0.0001$), Aβ RA-LTMRs ($p = 0.0006$), and Aβ Field-LTMRs ($p < 0.0001$), suggesting I_{mech} in C-LTMRs decays slower. Kruskal-Wallis test with Dunn's multiple comparisons test. n = 12 for C-LTMRs, n = 11 for Aδ-LTMRs; n = 13 for Aβ RA-LTMRs; n = 8 for Aβ SA1-LTMRs; n = 15 for Aβ Field-LTMRs and n = 11 for proprioceptors.

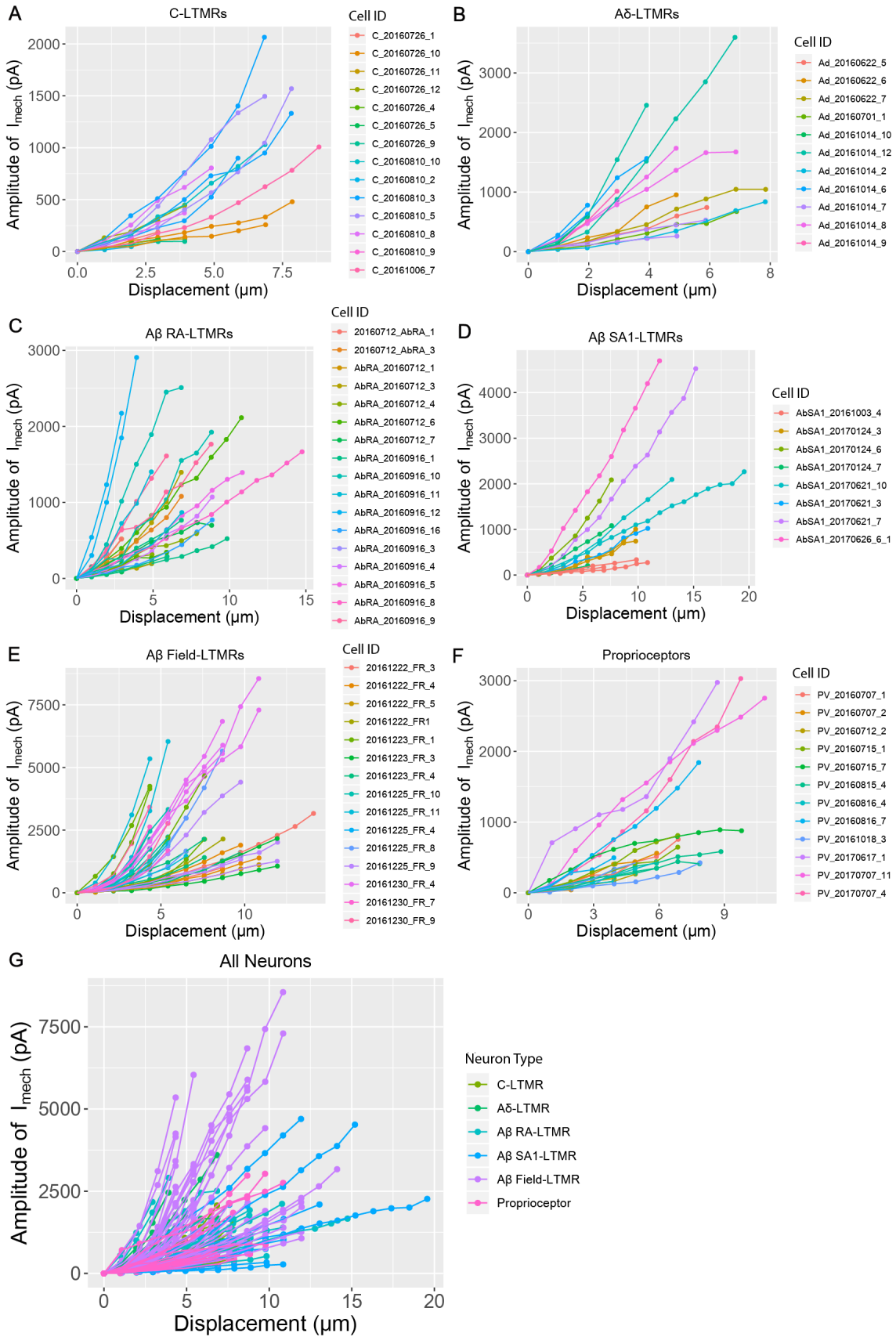
A
C-LTMRs
Amplitude of I_{mech} (pA)
Displacement (μm)
Cell ID
C_20160726_1
C_20160726_10
C_20160726_11
C_20160726_12
C_20160726_4
C_20160726_5
C_20160726_9
C_20160810_10
C_20160810_2
C_20160810_3
C_20160810_5
C_20160810_8
C_20160810_9
C_20161006_7
B
Aδ-LTMRs
Amplitude of I_{mech} (pA)
Displacement (μm)
Cell ID
Ad_20160622_5
Ad_20160622_6
Ad_20160622_7
Ad_20160701_1
Ad_20161014_10
Ad_20161014_12
Ad_20161014_2
Ad_20161014_6
Ad_20161014_7
Ad_20161014_8
Ad_20161014_9
C
Aβ RA-LTMRs
Amplitude of I_{mech} (pA)
Displacement (μm)
Cell ID
20160712_AbRA_1
20160712_AbRA_3
AbRA_20160712_1
AbRA_20160712_3
AbRA_20160712_4
AbRA_20160712_6
AbRA_20160712_7
AbRA_20160916_1
AbRA_20160916_10
AbRA_20160916_11
AbRA_20160916_12
AbRA_20160916_16
AbRA_20160916_3
AbRA_20160916_4
AbRA_20160916_5
AbRA_20160916_8
AbRA_20160916_9
D
Aβ SA1-LTMRs
Amplitude of I_{mech} (pA)
Displacement (μm)
Cell ID
AbSA1_20161003_4
AbSA1_20170124_3
AbSA1_20170124_6
AbSA1_20170124_7
AbSA1_20170621_10
AbSA1_20170621_3
AbSA1_20170621_7
AbSA1_20170626_6_1
E
Aβ Field-LTMRs
Amplitude of I_{mech} (pA)
Displacement (μm)
Cell ID
20161222_FR_3
20161222_FR_4
20161222_FR_5
20161222_FR1
20161223_FR_1
20161223_FR_3
20161223_FR_4
20161225_FR_10
20161225_FR_11
20161225_FR_4
20161225_FR_8
20161225_FR_9
20161230_FR_4
20161230_FR_7
20161230_FR_9
F
Proprioceptors
Amplitude of I_{mech} (pA)
Displacement (μm)
Cell ID
PV_20160707_1
PV_20160707_2
PV_20160712_2
PV_20160715_1
PV_20160715_7
PV_20160815_4
PV_20160816_4
PV_20160816_7
PV_20161018_3
PV_20170617_1
PV_20170707_11
PV_20170707_4
G
All Neurons
Amplitude of I_{mech} (pA)
Displacement (μm)
Neuron Type
C-LTMR
Aδ-LTMR
Aβ RA-LTMR
Aβ SA1-LTMR
Aβ Field-LTMR
Proprioceptor

Figure 2.2.2. Relationship between amplitude of I_{mech} and size of displacement

(**A**-**F**) Scatter plot displaying amplitude of I_{mech} (pA) against size of displacement (μm) in C-LTMRs (**A**), Aδ-LTMRs (**B**); Aβ RA-LTMRs (**C**); Aβ SA1-LTMRs (**D**); Aβ Field-LTMRs (**E**) and proprioceptors (**F**). n = 14 for C-LTMRs, n = 11 for Aδ-LTMRs; n = 17 for Aβ RA-LTMRs; n = 8 for Aβ SA1-LTMRs; n = 15 for Aβ Field-LTMRs and n = 12 for proprioceptors. Dots connected by lines represent data obtained from one recording with different mechanical step stimulations. Dots of the same color represent data obtained from the same neuron. Lines (and dots connected by the lines) of the same color represent data acquired from different recordings but from the same neuron. Zero point was defined as the last data point where I_{mech} is closest to 100 pA (difference between I_{mech} and 100 pA is smallest) before I_{mech} consistently increases. Coordinates of all other points were calculated by subtraction of the absolute coordinates of the zero point from their absolute coordinates. Neurons that have maximum I_{mech} amplitude around 100 pA are filtered out. I_{mech}-displacement curve shows that I_{mech} did not saturate, and the slope varies among neurons.

(**G**) Scatter plot displaying amplitude of I_{mech} (pA) against size of displacement (μm) of all neurons. Data are a combination of all the data from (**A**-**F**).

Taken together, these in vitro electrophysiological recordings indicate that most functionally distinct DRG neuron subtypes are distinguished by unique combinations of firing patterns, AP waveforms, and mechanical sensitivities; Aβ Field-LTMRs and Aβ SA1-LTMRs displayed remarkably similar intrinsic properties despite major differences in their *in vivo* responses to mechanical stimuli acting on the skin, which is likely attributed to their unique peripheral terminal morphologies and the skin cell types with which they associate. Differences in intrinsic physiological properties among the subtypes are likely due to differences in ion channels and components of the mechanotransduction machinery that they express.

CHAPTER 3. EXPERIMENTAL RESULTS

Deep RNA-Sequencing Reveals Gene Expression Patterns in Eight DRG Neuron Subtypes

3.1. Deep RNA-sequencing generates transcriptome profiles of major DRG neuron subtypes

To begin to explore the molecular basis of the distinct intrinsic membrane properties and other distinguishing features of DRG neuron subtypes, we undertook an RNA-sequencing approach to generate transcriptome profiles for each of the eight major DRG neuron subtypes. We made use of the aforementioned genetic tools that selectively label each of these subtypes with fluorescent reporters, first purifying labeled neurons to homogeneity using flow cytometry (FACS) and then extracting RNA from these purified neuronal populations (Table 2.1.1 and Figure 3.1.1 A). DRGs from multiple animals were combined for FACS, and neurons from multiple rounds of sorting were combined to obtain sufficient amounts of RNA for each sequencing reaction. At least three biological replicates were sequenced for each neuronal subtype (Figure 3.1.1 A). RNA libraries were prepared and subsequently sequenced using an Illumina HiSeq2000 platform at an average depth of ~75 million mapped reads per sample. This depth translates to an average detection level of 12,226 genes per sample (See Experimental Procedures). By using well characterized mouse lines for specific labeling of neuronal subtypes, this analysis links gene expression patterns to sensory neuron subtypes defined by their distinct *in vivo* properties as well as their corresponding intrinsic properties, described above. This is particularly important for the three Aβ-LTMR subtypes, which account for

low percentages of DRG neurons and have not been previously captured or distinguished by single cell sequencing approaches (Usoskin et al., 2015). Moreover, bulk RNA-sequencing at the high depth afforded by our analysis approaches or reaches saturation of gene detection, including the detection of low-expressed genes such as ion channels, more accurately measures gene expression differences across subtypes, and facilitates identification of differentially expressed genes (DEGs) (Li et al., 2016). Using this deep sequencing strategy, we generated a count matrix of the expression of all genes for each of the eight major DRG neuron subtypes.

The count matrix was transformed using a regularized logarithm (rlog) implemented in DESeq2 and thus rendered homoscedastic (Love et al., 2014). Unsupervised hierarchical clustering and principal component analysis (PCA), using rlog values as measures of gene expression, showed that biological replicates for the same neuronal subtype cluster with each other (see Experimental Procedures, Figure 3.1.1 B-D). This finding suggests that differences in gene expression across neuronal subtypes are not masked by variations across sequencing batches or noise introduced by experimental procedures.

We assessed the validity of the transcriptome profiles by examining expression patterns of several marker genes, including genes employed for the genetic tools and those whose expression patterns are well established in the DRG, as well as subtype-uniquely enriched genes (SUEGs) (See Experimental Procedures for identification of SUEGs). For the former, expression patterns of several marker genes were found to be consistent with established knowledge (Figure 3.1.2 B). For the latter, many SUEGs found in $MrgD^{+}$

polymodal nociceptors, $CGRP^{+}$ peptidergic nociceptors, C-LTMRs, and proprioceptors are in agreement with prior single-cell sequencing studies that identified these subtypes (data not shown) (Usoskin et al., 2015). Importantly, many SUEGs found in Aβ RA-LTMRs, Aβ SA1-LTMRs, and Aβ Field-LTMRs, including those encoding ion channels, were identified here for the first time, underscoring the benefit of this deep sequencing strategy, compared to prior single cell sequencing analyses, for resolving differences in lowly expressed genes. Several SUEGs were also selected for validation by double immunostaining, double fluorescent *in situ* hybridization (Figure 3.1.3), and through characterization of a new mouse genetic tool (*Calb1*^{dgCre}), which preferentially labels Aβ RA-LTMRs (Figure 3.1.4). The deep transcriptome analysis of each of the eight major DRG neuron subtypes thus allows for the identification of gene candidates underlying subtype specific properties, including intrinsic physiological properties.

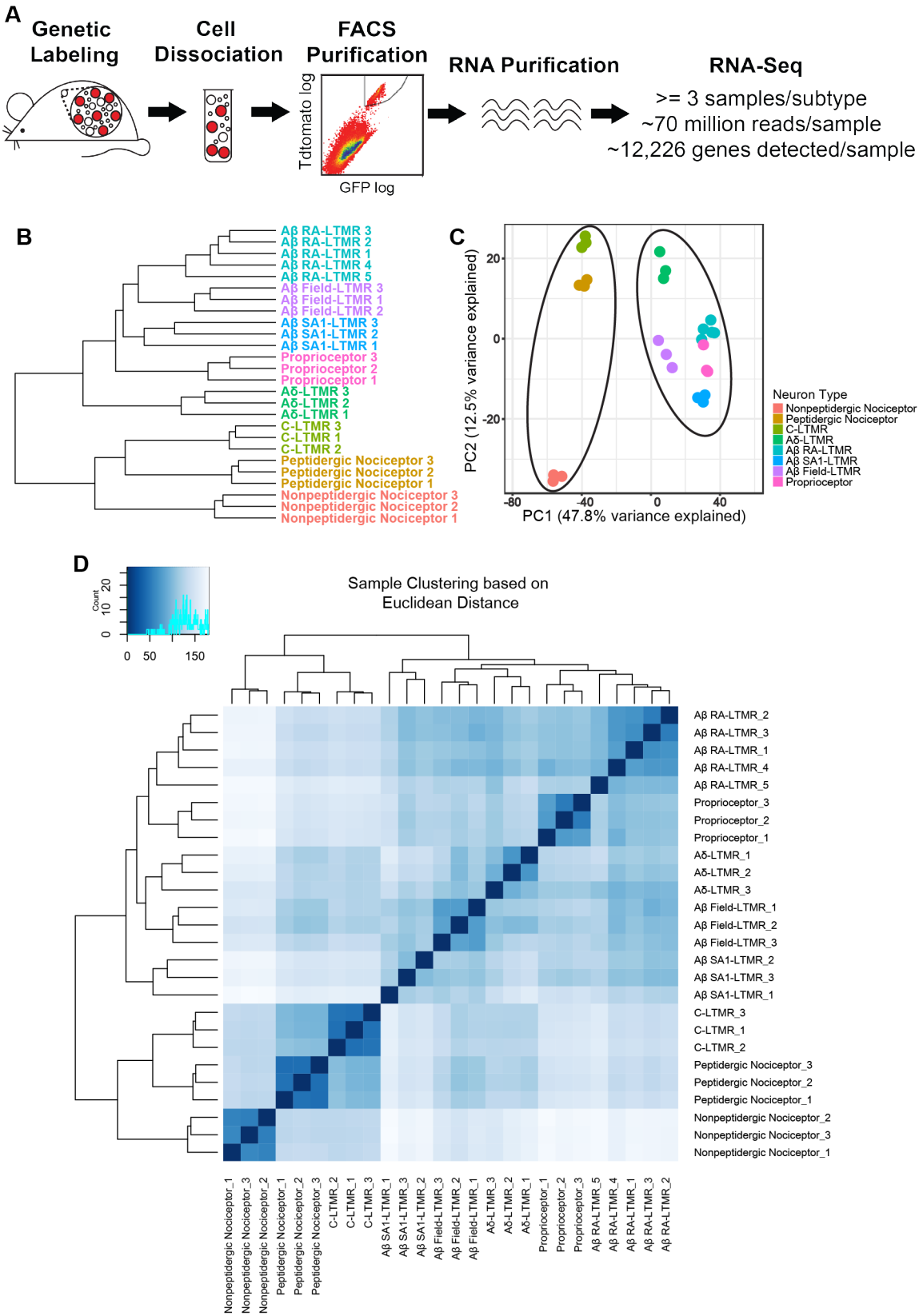
A
Genetic Labeling
Cell Dissociation
FACS Purification
RNA Purification
RNA-Seq
Tdtomato log
GFP log
>= 3 samples/subtype
~70 million reads/sample
~12,226 genes detected/sample
B
Aβ RA-LTMR 3
Aβ RA-LTMR 2
Aβ RA-LTMR 1
Aβ RA-LTMR 4
Aβ RA-LTMR 5
Aβ Field-LTMR 3
Aβ Field-LTMR 1
Aβ Field-LTMR 2
Aβ SA1-LTMR 3
Aβ SA1-LTMR 2
Aβ SA1-LTMR 1
Proprioceptor 3
Proprioceptor 2
Proprioceptor 1
Aδ-LTMR 3
Aδ-LTMR 2
Aδ-LTMR 1
C-LTMR 3
C-LTMR 1
C-LTMR 2
Peptidergic Nociceptor 3
Peptidergic Nociceptor 2
Peptidergic Nociceptor 1
Nonpeptidergic Nociceptor 3
Nonpeptidergic Nociceptor 2
Nonpeptidergic Nociceptor 1
C
PC2 (12.5% variance explained)
PC1 (47.8% variance explained)
Neuron Type
Nonpeptidergic Nociceptor
Peptidergic Nociceptor
C-LTMR
Aδ-LTMR
Aβ RA-LTMR
Aβ SA1-LTMR
Aβ Field-LTMR
Proprioceptor
D
Count
Sample Clustering based on Euclidean Distance
Aβ RA-LTMR_2
Aβ RA-LTMR_3
Aβ RA-LTMR_1
Aβ RA-LTMR_4
Aβ RA-LTMR_5
Proprioceptor_3
Proprioceptor_2
Proprioceptor_1
Aδ-LTMR_1
Aδ-LTMR_2
Aδ-LTMR_3
Aβ Field-LTMR_1
Aβ Field-LTMR_2
Aβ Field-LTMR_3
Aβ SA1-LTMR_2
Aβ SA1-LTMR_3
Aβ SA1-LTMR_1
C-LTMR_3
C-LTMR_1
C-LTMR_2
Peptidergic Nociceptor_3
Peptidergic Nociceptor_2
Peptidergic Nociceptor_1
Nonpeptidergic Nociceptor_2
Nonpeptidergic Nociceptor_3
Nonpeptidergic Nociceptor_1

Figure 3.1.1. Schematic of the RNA-sequencing workflow.

(A) Schematic of the RNA-sequencing workflow in this study.

(**B**) Hierarchical clustering of samples based on the expression of the top 1000 genes that display the highest expression variance across samples. Distance is calculated using the Euclidean method.

(C) Principle component analysis (PCA) of samples based on the expression of the top 1000 genes that display the highest expression variance across samples. Distance is calculated using the Euclidean method.

(**D**) Heatmap with hierarchical clustering of samples based on all gene expression shows that samples from the same neuronal subtype clusters together.

(**B-D**) Expression level is reported as the rlog transformed count values. All three analyses show that 1) samples from the same neuronal subtype cluster with each other, and 2) samples form two major clusters, $MrgD^+$ nonpeptidergic nociceptors, $CGRP^+$ peptidergic nociceptors and C-LTMRs as one cluster, Aδ-LTMRs, three Aβ-LTMR subtypes and proprioceptors as the other cluster, as shown in (**C**). The two major cluster patterns are consistent using PCA analysis on expression of all genes or hierarchical clustering with expression of all genes (data not shown).

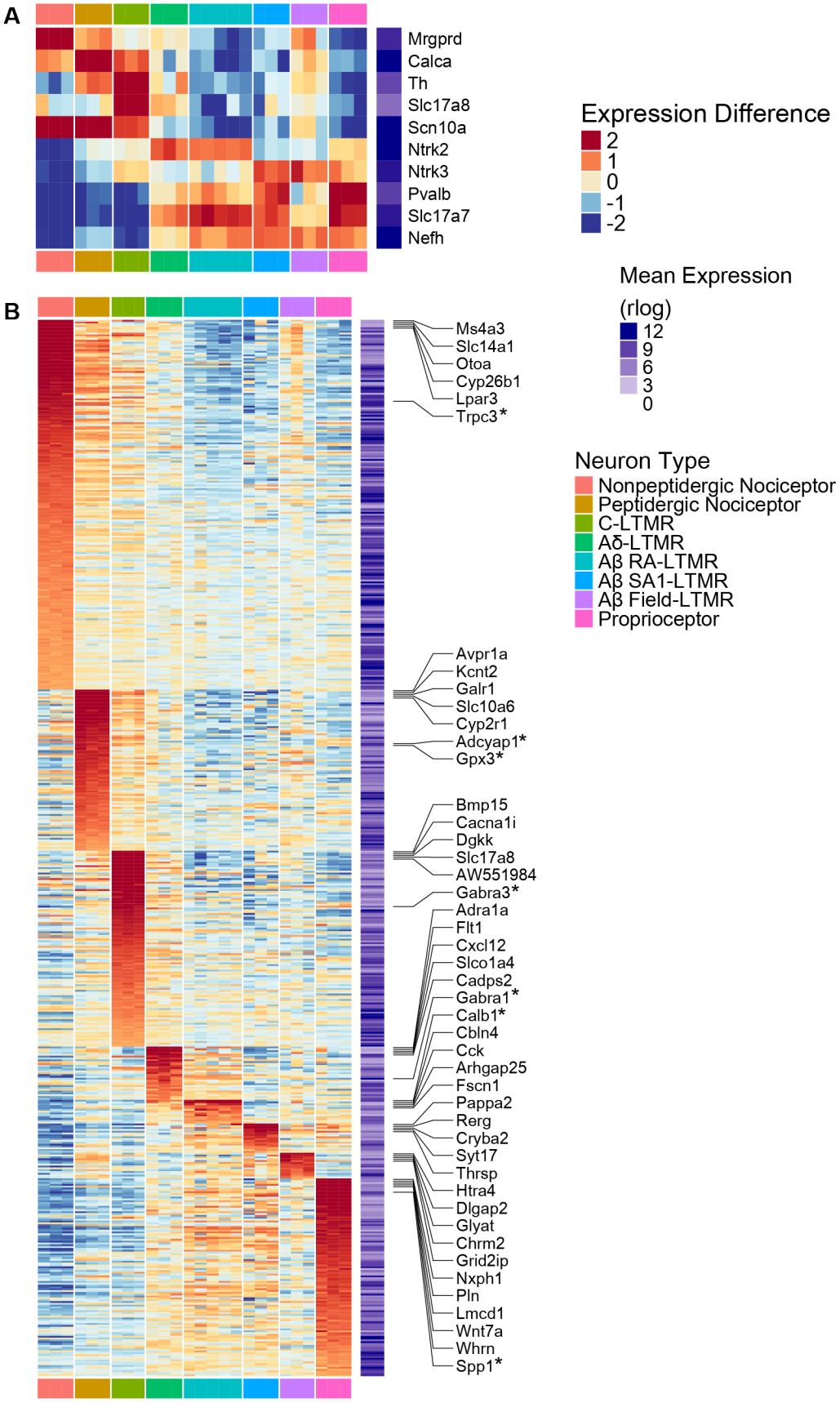
A
Mrgprd
Calca
Th
Slc17a8
Scn10a
Ntrk2
Ntrk3
Pvalb
Slc17a7
Nefh
Expression Difference
2
1
0
-1
-2
B
Mean Expression
(rlog)
12
9
6
3
0
Ms4a3
Slc14a1
Otoa
Cyp26b1
Lpar3
Trpc3*
Avpr1a
Kcnt2
Galr1
Slc10a6
Cyp2r1
Adcyap1*
Gpx3*
Bmp15
Cacna1i
Dgkk
Slc17a8
AW551984
Gabra3*
Adra1a
Flt1
Cxcl12
Slco1a4
Cadps2
Gabra1*
Calb1*
Cbln4
Cck
Arhgap25
Fscn1
Pappa2
Rerg
Cryba2
Syt17
Thrsp
Htra4
Dlgap2
Glyat
Chrm2
Grid2ip
Nxph1
Pln
Lmcd1
Wnt7a
Whrn
Spp1*
Neuron Type
Nonpeptidergic Nociceptor
Peptidergic Nociceptor
C-LTMR
Aδ-LTMR
Aβ RA-LTMR
Aβ SA1-LTMR
Aβ Field-LTMR
Proprioceptor

Figure 3.1.2. Expression patterns of marker genes and SUEGs.

(**A**) Heatmap showing expression patterns across subtypes (columns) of established marker genes (rows), including genes used for generating mouse tools that are employed in this study for subtype-specific labeling (Mrgprd (MrgD), Calca (CGRP), Th (TH), Ntrk2 (TrkB), Ntrk3 (TrkC), Pvalb (PV)) and genes of which the expression patterns have been previously studied (Slc17a8 (vGlut3), Scn10a (Nav1.8), Slc17a7 (vGlut1), Nefh (NFH)). Npy2r-GFP mice used to label Aβ RA-LTMRs is a BAC transgenic mouse line, and GFP expression does not recapitulate endogenous Npy2r gene expression, therefore it is not included here. Expression deviation from average expression level for each gene is plotted. Expression levels were measured using rlog transformed count values. The average expression level was calculated by averaging expression levels across all samples and plotted in a separate heatmap column next to the main plot. An rlog difference of 1 roughly translates to a 2-fold change. For details of distribution of average expression levels, see Experimental Procedures.

(**B**) Heatmap depicting differential expression patterns of subtype uniquely enriched genes (SUEGs). Expression differences are compared to the average expression levels for each gene are plotted in the main heatmap. Average expression level was calculated by averaging expression levels across all samples, and is plotted in a second heatmap next to the main heatmap. Expression levels were measured using rlog transformed count values. Only highly expressed genes (average expression in the 75^{th} percentile) were selected for this analysis. Genes are ordered based on the subtype in which their expression is enriched, and their degree of enrichment (expression differences compared to average

expression levels). The top five most enriched genes for each of the neuronal subtypes are labeled. Genes whose expression were further tested using experimental measures as shown in Figure 3.1.3 are labeled and marked with an asterisk.

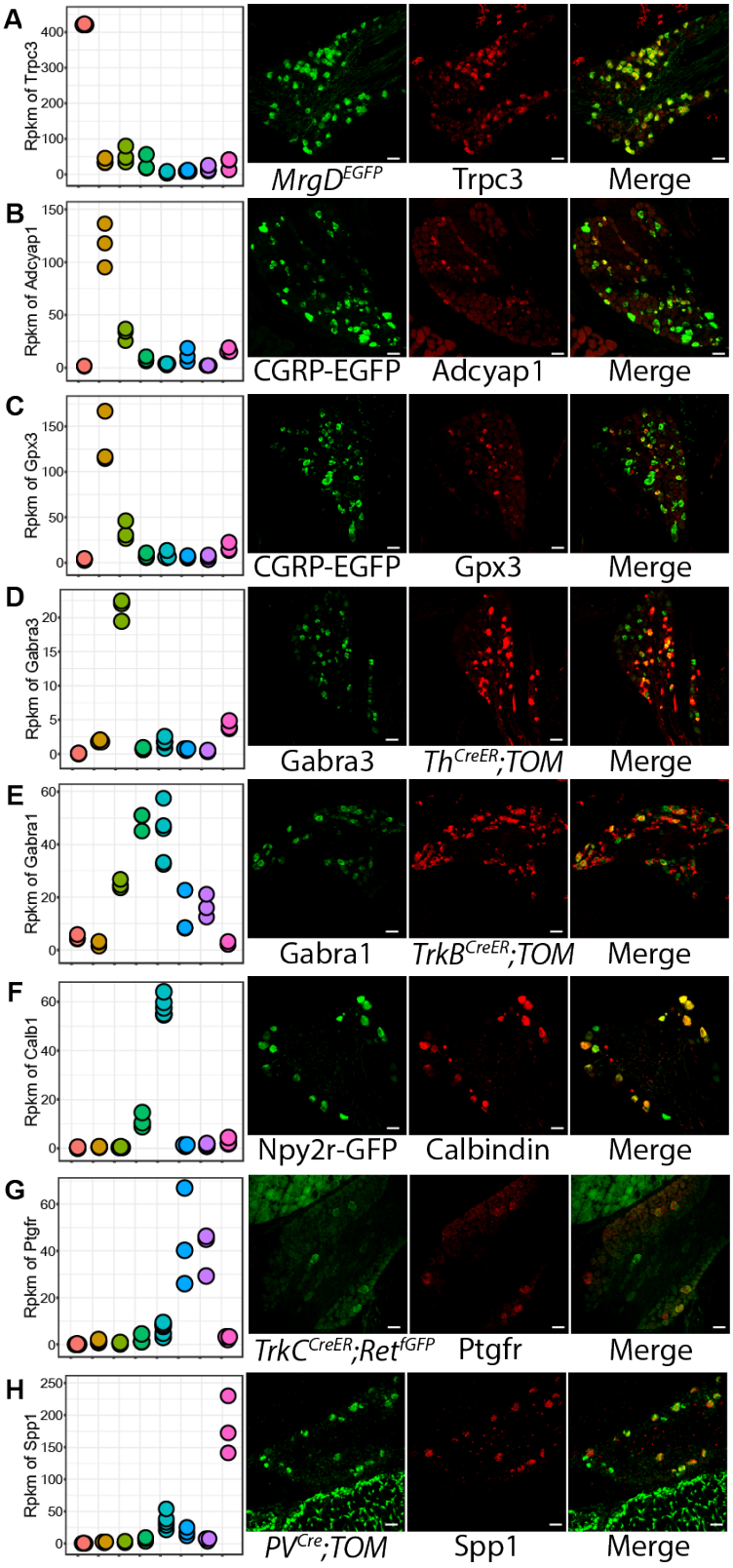
A
Rpkm of Trpc3
400
300
200
100
0
MrgD^EGFP
Trpc3
Merge
B
Rpkm of Adcyap1
150
100
50
0
CGRP-EGFP
Adcyap1
Merge
C
Rpkm of Gpx3
150
100
50
0
CGRP-EGFP
Gpx3
Merge
D
Rpkm of Gabra3
20
15
10
5
0
Gabra3
Th^CreER;TOM
Merge
E
Rpkm of Gabra1
60
40
20
0
Gabra1
TrkB^CreER;TOM
Merge
F
Rpkm of Calb1
60
40
20
0
Npy2r-GFP
Calbindin
Merge
G
Rpkm of Ptgfr
60
40
20
0
TrkC^CreER;Ret^fGFP
Ptgfr
Merge
H
Rpkm of Spp1
250
200
150
100
50
0
PV^Cre;TOM
Spp1
Merge

Figure 3.1.3. Experimental verification of selected genes using immunohistochemistry or *in situ* hybridization.

(**A**-**H**) Left-most panels: Dot plots depicting the level of expression of selected genes across subtypes using rpkm values (reads per kilobase per million reads). Three right panels: Representative images of double immunostaining (**A**, **D**, **E**, **F**) or *in situ* hybridization (**B**, **C**, **G**, **H**) of sensory neuron reporters and select genes using sections of DRGs from genetically labeled mice. Sensory neuron subtype reporters and tested genes are shown in separate channels, and the degree of overlap between the two is shown in the merged images. ($n \geqslant 2$ mice for each gene and see Experimental Procedures for further details).

Calb1^{dgCre};*Avil*^{FlpO};*R26*$^{LSL\text{-}FSF\text{-}tdTomato}$ TMP100 µg/g x 2 days (P18,19)

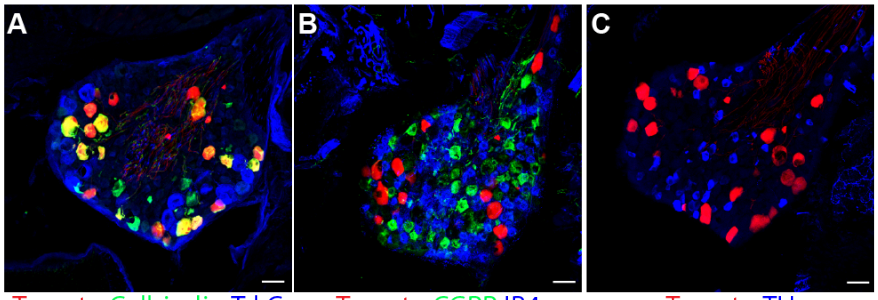

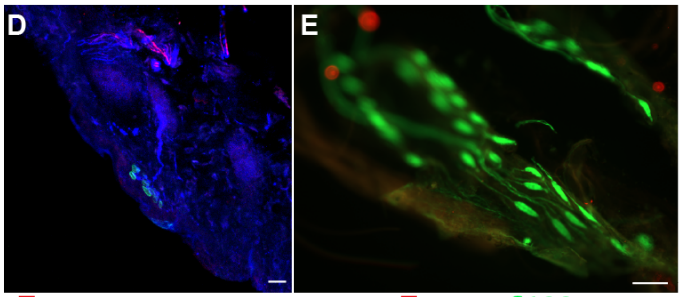

F *Calb1*^{dgCre};*R26*$^{LSL\text{-}tdTomato}$;*TrkB*^{GFP}
TMP100 µg/g x 2 days (P18,19)

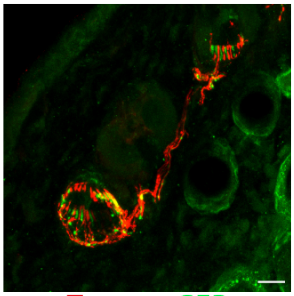

G

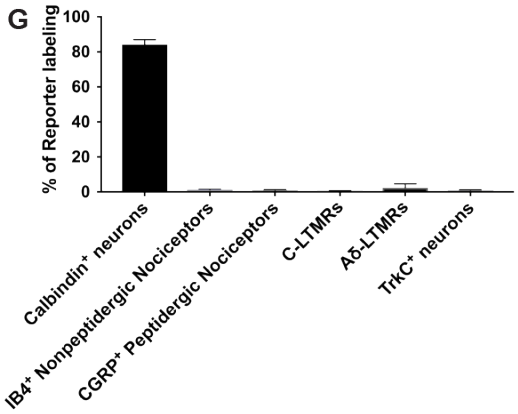

H *Calb1*^{dgCre};*Brn3a*^{AP}
TMP100 µg/g x 2 days (P18,19)

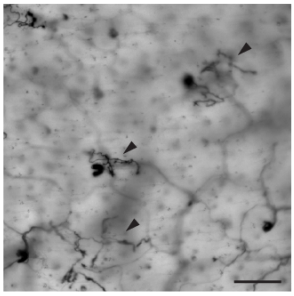

Figure 3.1.4. RNA-sequencing yields a new genetic strategy employing *Calb1^{dgCre}* to label Aβ RA-LTMRs.

(**A-C**) DRG sections from *Calb1^{dgCre}; Advillin^{FlpO}; R26$^{LSL-FSF-tdTomato}$* (Ai65) animals treated with TMP at P18,19, show that the majority tdTomato^{+} neurons express Calbindin (84.2±2.8%, n = 4 animals), but do not express markers of other sensory neuron subtypes, IB4 (1.18±0.5%, n = 4 animals), CGRP (0.93±0.4%, n = 4 animals), TH (0.4±0.4%, n = 4 animals), TrkC (0.9±0.3%, n = 4 animals).

(**D**) An example of skin sections showing that tdTomato^{+} endings are not associated with Merkel cells (n > 200 clusters of merkel cells and Aβ SA1-LTMRs from n = 3 animals are examined).

(**E**) An example of whole mount staining of periosteum membrane showing that tdTomato^{+} endings are not associated with Pacinian corpuscles (8 periosteum membranes from n = 4 animals are examined).

(**F**) An example of skin sections from *Calb1^{dgCre}; R26$^{LSL-tdTomato}$; TrkB^{GFP}* showing that tdTomato^{+} endings are GFP^{-} lanceolate endings (overlap < 3%, n = 3 animals), and are therefore not Aδ-LTMRs.

(**G**) Percentage of tdTomato^{+} DRG neurons or endings that express other molecular markers, as shown in (**A-C** and **F**). Data are represented as mean ± SEM.

(**H**) An example of whole mount back hairy skin staining from an *Calb1*^{dgCre}*; Brn3a*$^{f(AP)}$ animal showing that the majority of AP^{+} endings are lanceolate endings, though occasionally AP^{+} free nerve endings were seen.

Scale bars, (**A**-**C**) 50 μm, (**E**, **H**) 200 μm, (**D**, **F**) 20 μm.

3.2. Functionally relevant genes are differentially expressed across DRG neuron subtypes

In addition to differences in intrinsic physiological properties, DRG neuron subtypes differ in their developmental trajectories, peripheral terminal morphologies, response properties, central projection patterns and postsynaptic partners, and modes of presynaptic modulation of their central terminals (Abraira and Ginty, 2013; Fleming and Luo, 2013; Zimmerman et al., 2014). To determine gene expression patterns that may underlie these and other subtype-specific properties, we next examined the expression patterns of genes that fall within six functionally relevant categories implicated in shaping neuronal phenotype. The gene categories explored are: transcription factors (TFs), cell adhesion molecules (CAMs), neuropeptides, synaptic exocytosis machinery, G protein-coupled receptors (GPCRs), and ion channels (Chawla et al., 2013; Földy et al., 2016; Paul et al., 2017; Südhof, 2012). Among the top 75% of expressed genes ranked by average rlog values, there are 511 transcription factors, 306 cell adhesion molecules, 183 GPCRs, 175 ion channel genes, 94 synaptic vesicle exocytosis genes and 23 neuropeptide genes. Genes from each of the categories are differentially expressed among the DRG neuron subtypes (Figure 3.2.1). The most dramatic differences in gene expression patterns were observed between small-diameter neuron subtypes ($MrgD^+$ nonpeptidergic nociceptors, $CGRP^+$ peptidergic nociceptors, and C-LTMRs) and medium/large-diameter subtypes (Aδ-LTMRs, the three Aβ-LTMR subtypes, and proprioceptors), which is consistent with the expression structure revealed by hierarchical clustering and PCA analysis (Figure 3.1.1 B-D). For example, most neuropeptide genes and several TRP channels, including TrpA, TrpM8, and TrpV1, are expressed at higher levels in the small

diameter neuron subtypes compared to large-diameter subtypes (Figure 3.2.2 A and C). In addition, most synaptic exocytosis machinery genes display elevated expression in either small-diameter or large-diameter neuron subtype clusters (Figure 3.2.2 B). On the other hand, expression differences between small-diameter neuron subtypes or between medium/large-diameter neuron subtypes are less dramatic, although many notable differences exist (Figure 3.2.1 and 3.1.2). These data also revealed many TFs, CAMs, receptors, and ion channels that are uniquely enriched in each of the three small-diameter neuron subtypes, Aδ-LTMRs and proprioceptors, however fewer genes in these families distinguish the three Aβ-LTMR subtypes, which likely contributed to the difficulty resolving Aβ-LTMR subtypes in prior single cell analyses.

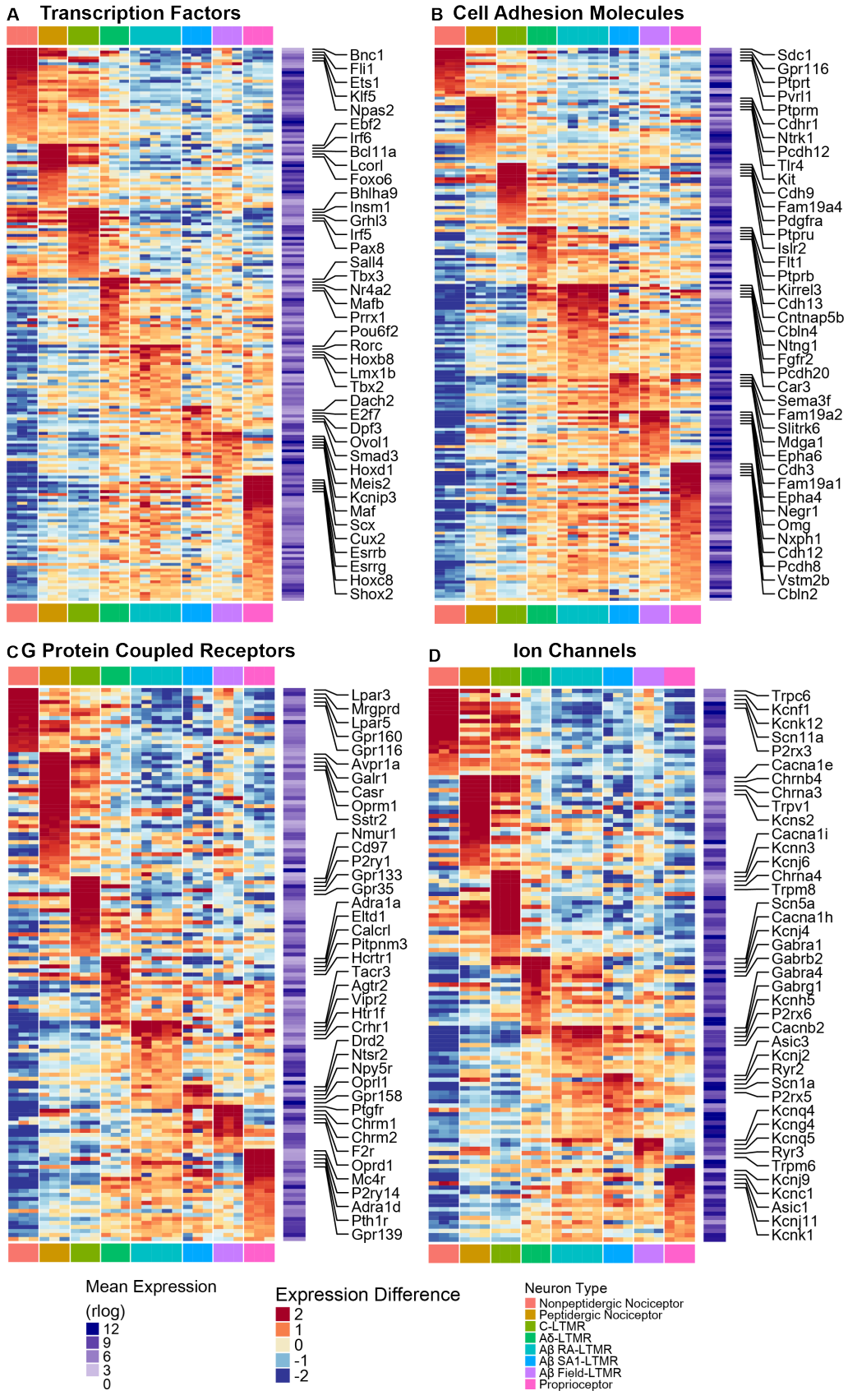
A Transcription Factors
Bnc1
Fli1
Ets1
Klf5
Npas2
Ebf2
Irf6
Bcl11a
Lcorl
Foxo6
Bhlha9
Insm1
Grhl3
Irf5
Pax8
Sall4
Tbx3
Nr4a2
Mafb
Prrx1
Pou6f2
Rorc
Hoxb8
Lmx1b
Tbx2
Dach2
E2f7
Dpf3
Ovol1
Smad3
Hoxd1
Meis2
Kcnip3
Maf
Scx
Cux2
Esrrb
Esrrg
Hoxc8
Shox2
B Cell Adhesion Molecules
Sdc1
Gpr116
Ptprt
Pvrl1
Ptprm
Cdhr1
Ntrk1
Pcdh12
Tlr4
Kit
Cdh9
Fam19a4
Pdgfra
Ptpru
Islr2
Flt1
Ptprb
Kirrel3
Cdh13
Cntnap5b
Cbln4
Ntng1
Fgfr2
Pcdh20
Car3
Sema3f
Fam19a2
Slitrk6
Mdga1
Epha6
Cdh3
Fam19a1
Epha4
Negr1
Omg
Nxph1
Cdh12
Pcdh8
Vstm2b
Cbln2
C G Protein Coupled Receptors
Lpar3
Mrgprd
Lpar5
Gpr160
Gpr116
Avpr1a
Galr1
Casr
Oprm1
Sstr2
Nmur1
Cd97
P2ry1
Gpr133
Gpr35
Adra1a
Eltd1
Calcrl
Pitpnm3
Hcrtr1
Tacr3
Agtr2
Vipr2
Htr1f
Crhr1
Drd2
Ntsr2
Npy5r
Oprl1
Gpr158
Ptgfr
Chrm1
Chrm2
F2r
Oprd1
Mc4r
P2ry14
Adra1d
Pth1r
Gpr139
D Ion Channels
Trpc6
Kcnf1
Kcnk12
Scn11a
P2rx3
Cacna1e
Chrnb4
Chrna3
Trpv1
Kcns2
Cacna1i
Kcnn3
Kcnj6
Chrna4
Trpm8
Scn5a
Cacna1h
Kcnj4
Gabra1
Gabrb2
Gabra4
Gabrg1
Kcnh5
P2rx6
Cacnb2
Asic3
Kcnj2
Ryr2
Scn1a
P2rx5
Kcnq4
Kcng4
Kcnq5
Ryr3
Trpm6
Kcnj9
Kcnc1
Asic1
Kcnj11
Kcnk1
Mean Expression
(rlog)
12
9
6
3
0
Expression Difference
2
1
0
-1
-2
Neuron Type
Nonpeptidergic Nociceptor
Peptidergic Nociceptor
C-LTMR
Aδ-LTMR
Aβ RA-LTMR
Aβ SA1-LTMR
Aβ Field-LTMR
Proprioceptor

Figure 3.2.1. Functionally relevant genes are differentially expressed across eight major DRG sensory neuron subtypes.

(**A-D**) Heatmaps depicting gene expression level differences for genes encoding transcription factors and transcriptional regulators (**A**), cell adhesion molecules (**B**), G protein-coupled receptors (**C**), and ion channels (**D**). Expression deviation from the average expression level is plotted in the heatmaps. Average expression level is plotted in the column next to the heatmaps. Only highly expressed genes (average expression in the 75^{th} percentile) in which at least three samples have an expression level deviation larger than 1 (most highly variable genes) were selected for these analyses. Gene expression was measured using rlog transformed count values.

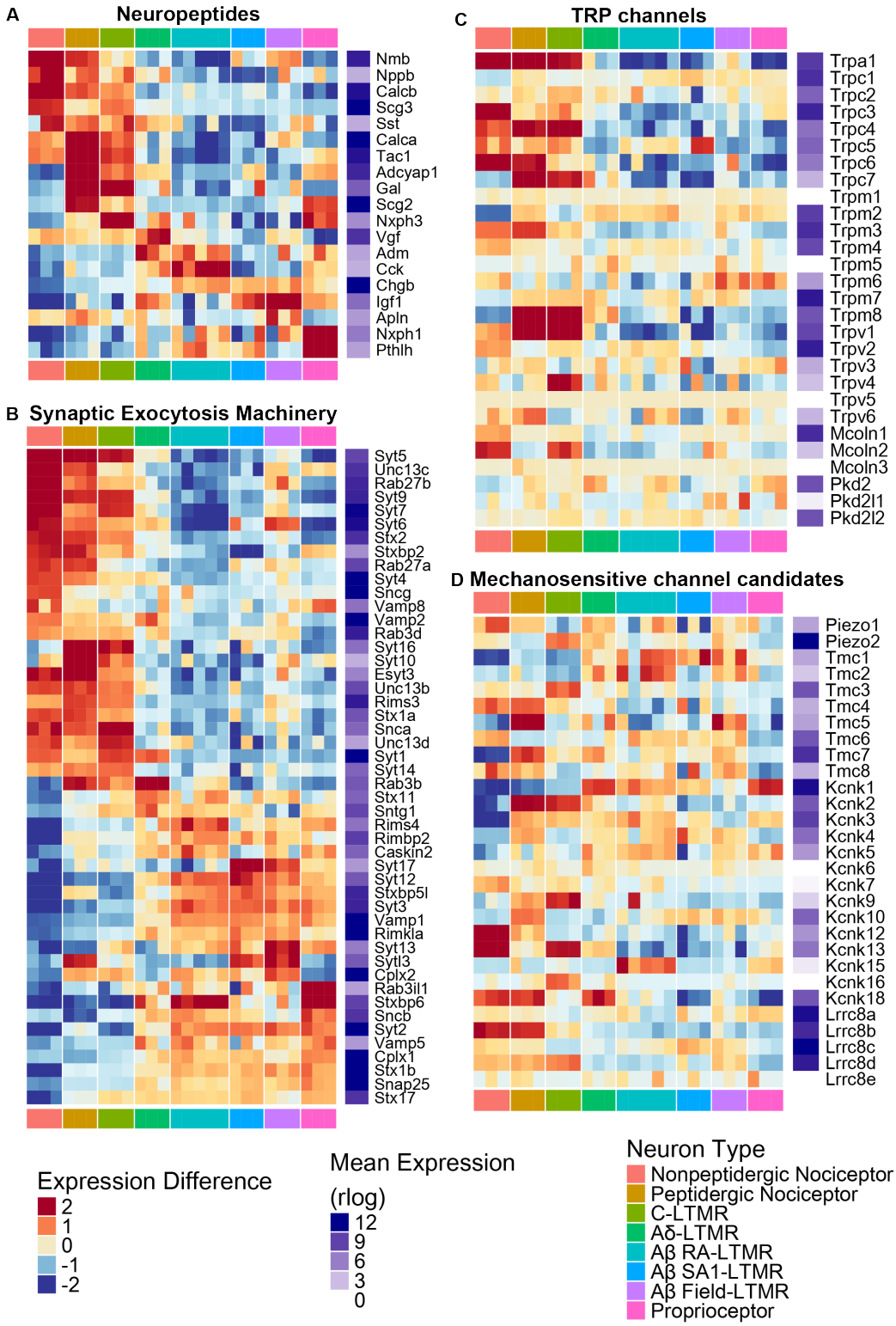
A
Neuropeptides
Nmb
Nppb
Calcb
Scg3
Sst
Calca
Tac1
Adcyap1
Gal
Scg2
Nxph3
Vgf
Adm
Cck
Chgb
Igf1
Apln
Nxph1
Pthlh
B
Synaptic Exocytosis Machinery
Syt5
Unc13c
Rab27b
Syt9
Syt7
Syt6
Stx2
Stxbp2
Rab27a
Syt4
Sncg
Vamp8
Vamp2
Rab3d
Syt16
Syt10
Esyt3
Unc13b
Rims3
Stx1a
Snca
Unc13d
Syt1
Syt14
Rab3b
Stx11
Sntg1
Rims4
Rimbp2
Caskin2
Syt17
Syt12
Stxbp5l
Syt3
Vamp1
Rimkla
Syt13
Sytl3
Cplx2
Rab3il1
Stxbp6
Sncb
Syt2
Vamp5
Cplx1
Stx1b
Snap25
Stx17
C
TRP channels
Trpa1
Trpc1
Trpc2
Trpc3
Trpc4
Trpc5
Trpc6
Trpc7
Trpm1
Trpm2
Trpm3
Trpm4
Trpm5
Trpm6
Trpm7
Trpm8
Trpv1
Trpv2
Trpv3
Trpv4
Trpv5
Trpv6
Mcoln1
Mcoln2
Mcoln3
Pkd2
Pkd2l1
Pkd2l2
D
Mechanosensitive channel candidates
Piezo1
Piezo2
Tmc1
Tmc2
Tmc3
Tmc4
Tmc5
Tmc6
Tmc7
Tmc8
Kcnk1
Kcnk2
Kcnk3
Kcnk4
Kcnk5
Kcnk6
Kcnk7
Kcnk9
Kcnk10
Kcnk12
Kcnk13
Kcnk15
Kcnk16
Kcnk18
Lrrc8a
Lrrc8b
Lrrc8c
Lrrc8d
Lrrc8e
Expression Difference
2
1
0
-1
-2
Mean Expression
(rlog)
12
9
6
3
0
Neuron Type
Nonpeptidergic Nociceptor
Peptidergic Nociceptor
C-LTMR
Aδ-LTMR
Aβ RA-LTMR
Aβ SA1-LTMR
Aβ Field-LTMR
Proprioceptor

Figure 3.2.2. Expression patterns of genes grouped by potential functions, Related to Figure 3.2.1.

(**A-D**) Heatmap of expression differences for genes encoding neuropeptides (**A**), synaptic exocytosis machinery proteins (**B**), TRP channels (**C**), and channels implicated in mechanosensation (**D**). As in Figure 3.2.1, expression differences compared to the average expression level for each gene are plotted in the main heatmap. Average expression levels were calculated by averaging expression levels across all samples, and plotted in a second heatmap next to the main plot. Expression levels were measured using rlog transformed count values. For **A** and **B**, only highly expressed genes (average expression in the 75th percentile) whose expression is most highly variable (at least three samples have expression deviation larger than 1) were selected for analyses. Genes are ordered based on the subtype in which they are most highly expressed, and their degree of enrichment (expression difference from the average expression level). For **C** and **D**, no filter was implemented and genes are arranged in alphabetical order.

3.3. Expression patterns of ion channel genes in DRG neuron subtypes

Our transcriptome profile data resolve patterns and levels of expression of each of the staggering number of genes encoding the principal or α subunits and auxiliary subunits of voltage-gated ion channels expressed in the DRG. This information provides a valuable guide for revealing the molecular identity of the ion channels that underlie subtype-specific intrinsic membrane properties and firing patterns, defined in experiments shown in Figure 2.1.1 and Figure 2.1.2. Therefore, we focused on the patterns of expression of voltage-gated ion channels for each major DRG neuron subtype.

Nav channel α subunit genes show a clear distinction among the neuronal subtypes (Figure 3.3.1 A). The most highly expressed Nav channels are Nav1.1, Nav1.6, Nav1.7, Nav1.8 and Nav1.9. Nav1.7 is expressed across all subtypes, with the notable exception for proprioceptors. On the other hand, Nav1.8 and Nav1.9 are most highly expressed in small-diameter neuron subtypes, whereas Nav1.1 and Nav1.6 are abundant in Aδ-LTMRs, the three Aβ-LTMR subtypes, and proprioceptors, but very low or undetectable in the small-diameter neuron types.

K channel genes exhibit the greatest diversity among voltage-gated ion channels; there are over ninety K channel subunit genes in the mouse genome (Coetzee et al., 1999; Vacher et al., 2008) and many show remarkably different patterns of expression among the DRG neuron subtypes (Figure 3.1.1 B-L, Figure 3.3.2 A-D). The expression of many different types of K channels is consistent with previous recordings showing the presence of many components of K current in DRG neurons, with considerable heterogeneity

among neurons of different sizes (Everill et al., 1998; Gold et al., 1996). Within the Kv1 subfamily, Kv1.1 expression was found to be elevated in large-diameter neuron subtypes compared to small-diameter neuron subtypes (Figure 3.3.1B). The pattern of Kv1.1 expression was confirmed by immunostaining experiments: most $Kv1.1^+$ neurons are $NF200^+$, but they do not express MrgD or TH, markers of $MrgD^+$ polymodal nociceptors and C-LTMRs, respectively (Figure 3.3.2 J, K). Kv1.2 expression is also relatively high in the large-diameter neuronal subtypes, especially compared to $MrgD^+$ nonpeptidergic nociceptors, and, as with Kv1.1, this pattern was supported by immunostaining: most $Kv1.2^+$ neurons are $NF200^+$, and $Kv1.2^+$ neurons do not express MrgD (Figure 3.3.2 L). Kv1.6 expression, on the other hand, is elevated in the small-diameter neuron subtypes and low or undetectable in large-diameter subtypes. Moreover, at least one Kv2 channel family member is expressed relatively abundantly (rpkm $\geqslant$ 20) in each of the neuronal subtypes (Figure 3.3.1 C). Of the Kv3 channel family members, Kv3.1 and Kv3.3 are both enriched in the large-diameter neuron subtypes (Figure 3.3.1 D); Kv3.1 is particularly highly enriched in proprioceptors where it may be critical for their fast spiking property. Both peptidergic and nonpeptidergic nociceptors express Kv3.4 channels, consistent with recent electrophysiology, single-cell qPCR, and immunocytochemistry (Muqeem et al., 2018; Ritter et al., 2012, 2015). For the Kv4 channel family, Kv4.3 is uniquely and highly expressed in C-LTMRs (Figure 3.3.1 E); this pattern was verified by immunostaining using Kv4.3-specific antibodies (Figure 3.3.2 M).

Among other differentially expressed K channel α subunits and auxiliary subunit genes, BK and SK1 channels are elevated in $MrgD^{+}$ polymodal nociceptors (consistent with previous work showing enrichment of BK current in a subpopulation of nociceptors (Zhang et al., 2010)), and Kv7.4 is particularly enriched in Aδ-LTMRs, Aβ RA-LTMRs and Aβ Field-LTMRs (Figure 3.3.1 G and L). The latter observation is consistent with the finding that Kv7.4 protein is detected in lanceolate endings, circumferential endings, but not in Merkel cell associated endings (Heidenreich et al., 2012). The highly diverse patterns of expression of Kv5, Kv6, Kv8 and Kv9 family members (Figure 3.3.1 F, H, I) suggests that the complexity of K channel compositions among the DRG neuron subtypes is further increased by distinct heteromers formed between these 'electrically-silent' (modulatory) channel subunits and Kv2 channels (Bocksteins and Snyders, 2012).

Other voltage-gated ion channel genes, including Cav channels and HCN family members, are also differentially expressed among the eight major DRG neuron subtypes (Figure 3.3.2 E-I). Thus, each DRG neuronal subtype exhibits a unique combination of voltage-gated ion channels that together shape transduction of sensory information.

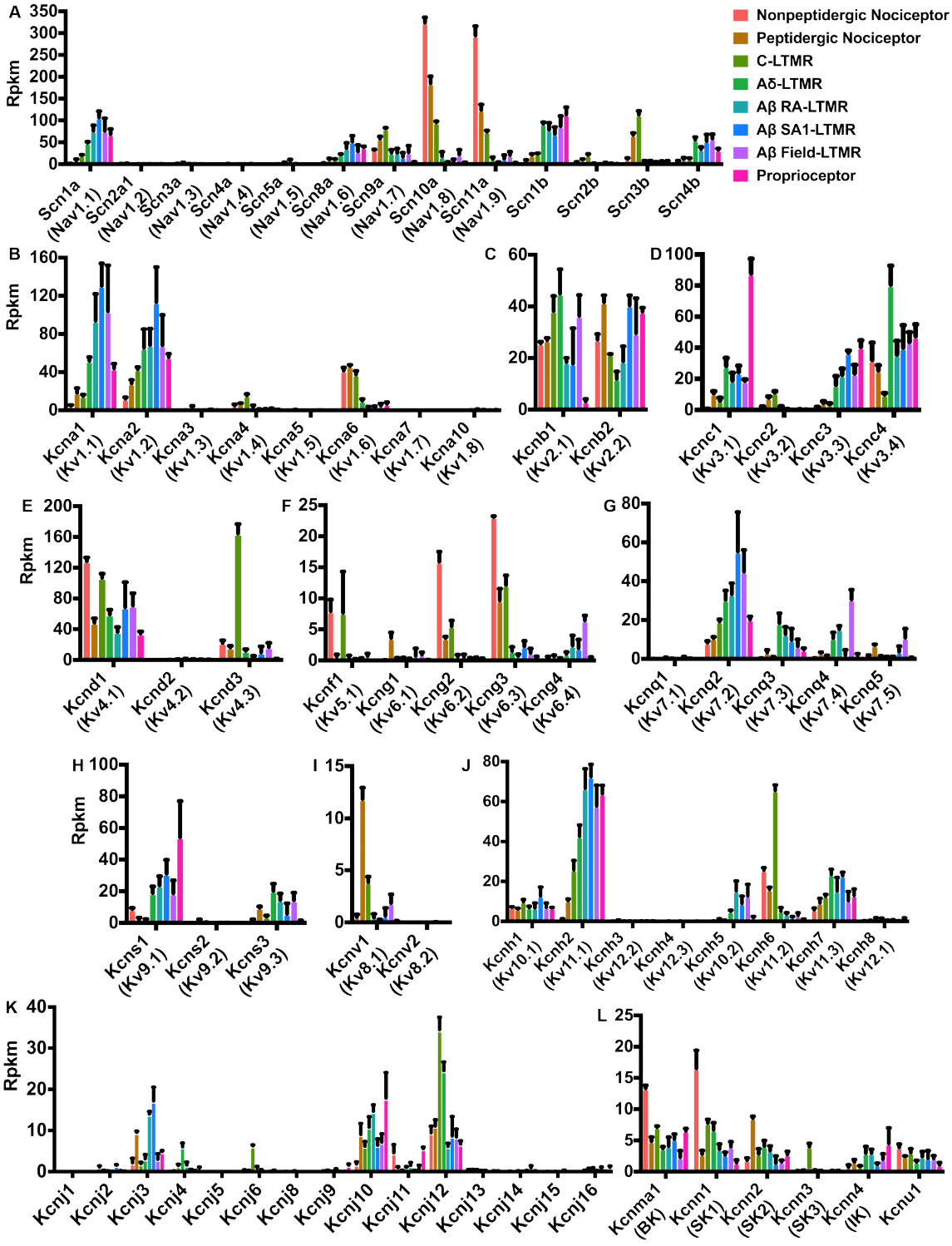
A
B
C
D
E
F
G
H
I
J
K
L
Rpkm
Nonpeptidergic Nociceptor
Peptidergic Nociceptor
C-LTMR
Aδ-LTMR
Aβ RA-LTMR
Aβ SA1-LTMR
Aβ Field-LTMR
Proprioceptor
Scn1a (Nav1.1)
Scn2a1 (Nav1.2)
Scn3a (Nav1.3)
Scn4a (Nav1.4)
Scn5a (Nav1.5)
Scn8a (Nav1.6)
Scn9a (Nav1.7)
Scn10a (Nav1.8)
Scn11a (Nav1.9)
Scn1b
Scn2b
Scn3b
Scn4b
Kcna1 (Kv1.1)
Kcna2 (Kv1.2)
Kcna3 (Kv1.3)
Kcna4 (Kv1.4)
Kcna5 (Kv1.5)
Kcna6 (Kv1.6)
Kcna7 (Kv1.7)
Kcna10 (Kv1.8)
Kcnb1 (Kv2.1)
Kcnb2 (Kv2.2)
Kcnc1 (Kv3.1)
Kcnc2 (Kv3.2)
Kcnc3 (Kv3.3)
Kcnc4 (Kv3.4)
Kcnd1 (Kv4.1)
Kcnd2 (Kv4.2)
Kcnd3 (Kv4.3)
Kcnf1 (Kv5.1)
Kcng1 (Kv6.1)
Kcng2 (Kv6.2)
Kcng3 (Kv6.3)
Kcng4 (Kv6.4)
Kcnq1 (Kv7.1)
Kcnq2 (Kv7.2)
Kcnq3 (Kv7.3)
Kcnq4 (Kv7.4)
Kcnq5 (Kv7.5)
Kcns1 (Kv9.1)
Kcns2 (Kv9.2)
Kcns3 (Kv9.3)
Kcnv1 (Kv8.1)
Kcnv2 (Kv8.2)
Kcnh1 (Kv10.1)
Kcnh2 (Kv11.1)
Kcnh3 (Kv12.2)
Kcnh4 (Kv12.3)
Kcnh5 (Kv10.2)
Kcnh6 (Kv11.2)
Kcnh7 (Kv11.3)
Kcnh8 (Kv12.1)
Kcnj1
Kcnj2
Kcnj3
Kcnj4
Kcnj5
Kcnj6
Kcnj8
Kcnj9
Kcnj10
Kcnj11
Kcnj12
Kcnj13
Kcnj14
Kcnj15
Kcnj16
Kcnma1 (BK)
Kcnn1 (SK1)
Kcnn2 (SK2)
Kcnn3 (SK3)
Kcnn4 (IK)
Kcnu1

Figure 3.3.1. Expression patterns of genes encoding Nav and Kv channel subunits. (**A-L**) Bar plots depicting gene expression levels of genes encoding voltage-gated sodium channel α and β subunits (**A**), Kv1 subunits (**B**), Kv2 subunits (**C**), Kv3 subunits (**D**), Kv4 subunits (**E**), Kv5 and Kv6 subunits (**F**), Kv7 subunits (**G**), Kv8 subunits (**I**), Kv9 subunits (**H**), Kv10 subunits (**J**), inward-rectifier potassium channel subunits (K_{ir}, IRK) (**K**) and calcium-activated potassium channel α subunits (**L**). Expression levels are reported using rpkm values. Shown are Data are represented as mean ± SD.

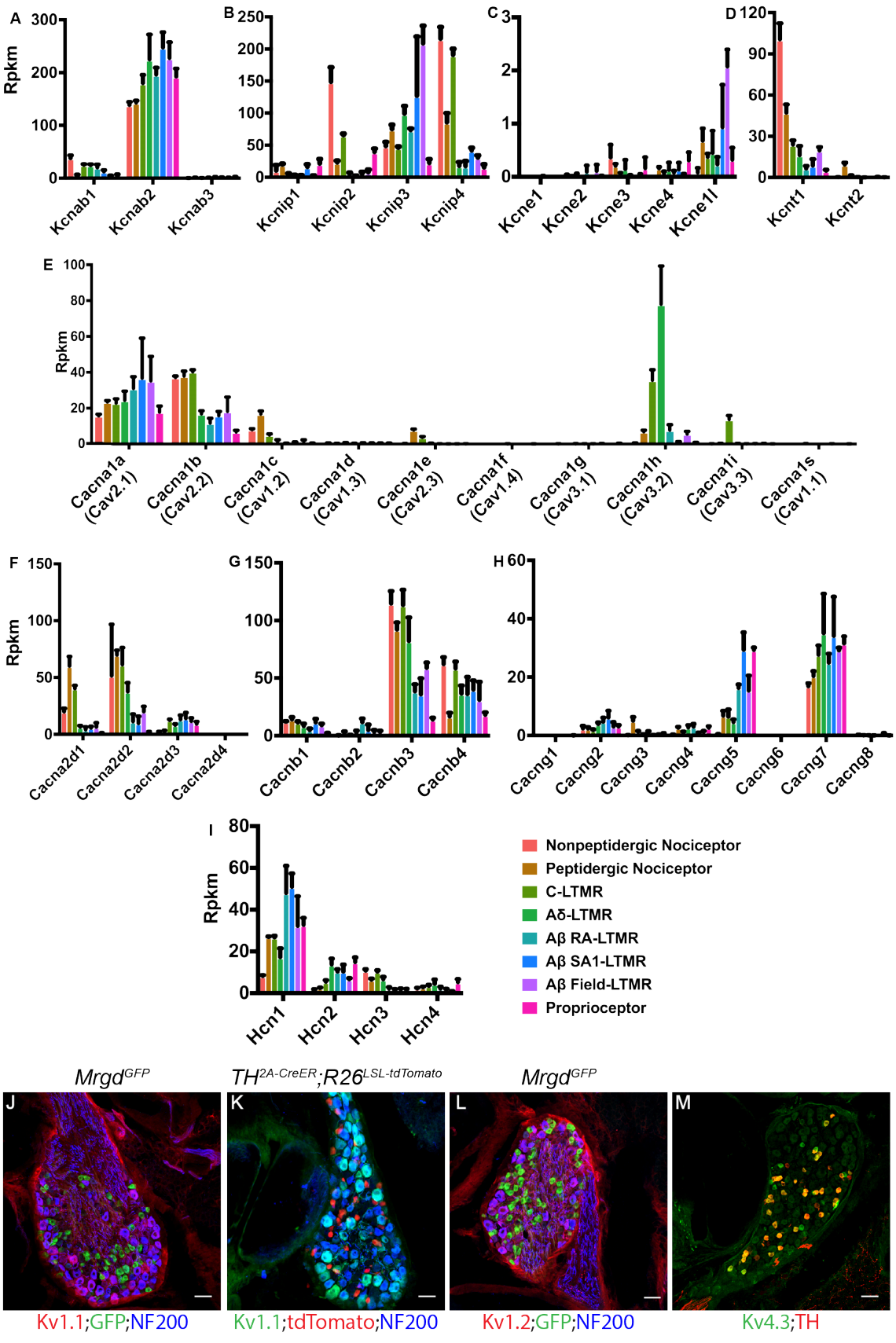
A
Rpkm
300
200
100
0
Kcnab1
Kcnab2
Kcnab3
B
250
200
150
100
50
0
Kcnip1
Kcnip2
Kcnip3
Kcnip4
C
3
2
1
0
Kcne1
Kcne2
Kcne3
Kcne4
Kcne1l
D
120
90
60
30
0
Kcnt1
Kcnt2
E
Rpkm
100
80
60
40
20
0
Cacna1a (Cav2.1)
Cacna1b (Cav2.2)
Cacna1c (Cav1.2)
Cacna1d (Cav1.3)
Cacna1e (Cav2.3)
Cacna1f (Cav1.4)
Cacna1g (Cav3.1)
Cacna1h (Cav3.2)
Cacna1i (Cav3.3)
Cacna1s (Cav1.1)
F
Rpkm
150
100
50
0
Cacna2d1
Cacna2d2
Cacna2d3
Cacna2d4
G
150
100
50
0
Cacnb1
Cacnb2
Cacnb3
Cacnb4
H
60
40
20
0
Cacng1
Cacng2
Cacng3
Cacng4
Cacng5
Cacng6
Cacng7
Cacng8
I
Rpkm
80
60
40
20
0
Hcn1
Hcn2
Hcn3
Hcn4
Nonpeptidergic Nociceptor
Peptidergic Nociceptor
C-LTMR
Aδ-LTMR
Aβ RA-LTMR
Aβ SA1-LTMR
Aβ Field-LTMR
Proprioceptor
MrgdGFP
TH2A-CreER;R26LSL-tdTomato
MrgdGFP
J
K
L
M
Kv1.1;GFP;NF200
Kv1.1;tdTomato;NF200
Kv1.2;GFP;NF200
Kv4.3;TH

Figure 3.3.2. Expression patterns of genes encoding voltage-gated ion channel subunits, Related to Figure 3.3.1.

(**A-H**) Bar plots showing expression levels of genes encoding voltage gated potassium channel subfamily A member regulatory β subunits (**A**), voltage-gated potassium channel-interacting proteins (KCNIPs) (**B**), voltage-gated potassium channel subfamily E regulatory β subunits (**C**), potassium channel subfamily T subunits (**D**), voltage-gated calcium channels α_1 subunits (**E**), $\alpha_2\delta$ subunits (**F**), β subunits (**G**) and γ subunits (**H**), and HCN channels (**I**). Expression levels are reported using rpkm values, and error bars represent mean ± SD.

(**I-J**) Representative images of immunolabeled DRG sections showing that most neurons expressing Kv1.1 also express NFH, but they are not $MrgD^+$ nonpeptidergic nociceptors or TH^+ C-LTMRs (n=3 mice).

(**K**) Representative images of DRG sections showing that most neurons expressing high level Kv1.2 also express NFH, but they are not $MrgD^+$ nonpeptidergic nociceptors (n=3 mice).

(**L**) Representative images of DRG sections showing that Kv4.3 expression largely overlaps with TH expression ($Kv4.3^+$ and TH^+/TH^+, 0.83 ± 0.03; Kv4.3 and $TH^+/Kv4.3^+$, 0.71 ± 0.05; n = 3 mice).

For (**C-F**), Scale bars, 50 μm.

CHAPTER 4. EXPERIMENTAL RESULTS

Differentially Expressed Potassium Channels Contribute to Membrane Properties in a Subtype-Distinct Manner

4.1. Major K channel families differentially contribute to outward potassium currents in a subtype-specific manner

The unique combinations of Kv channel expression patterns among DRG sensory neuron subtypes led us to hypothesize that differential expression of these particular ion channels is a key determinant of subtype-specific intrinsic physiological properties. The expression patterns of Kv1-Kv4 channels (Figure 4.1.1 A) suggest that Kv1, Kv2, Kv3, but not Kv4.3 may mediate large outward potassium currents in Aδ-LTMRs and Aβ-LTMRs. Another prediction is that Kv4.3, but not Kv3, carries large outward potassium current in C-LTMRs. To test these and other possibilities raised by the sequencing analysis, we next designed a whole-cell voltage-clamp experimental paradigm that combines the use of genetically labeled DRG neuron subtypes and pharmacological manipulations to quantitatively measure the contributions of Kv1, Kv2, Kv3 and Kv4 channels to total outward current.

We used a cumulative sequence of K channel inhibitors to quantify the magnitude of current carried by each class of Kv channels in each cell type. We quantified the fraction

---

The work described in this chapter represents a collaboration between Yang Zheng and Dr. Pin Liu. Dr. Pin Liu performed the *in vitro* voltage and current clamp electrophysiological experiments using genetically labeled or modified mice generated by Yang Zheng.

of each current involved in repolarizing the AP in each cell type by using previously-recorded AP waveforms in each DRG neuron subtype (Figure 2.1.1 and 2.2.2) as a voltage command. The channel inhibitor application protocol used inhibitors applied in a specific order and each with a concentration designed to achieve selective Kv channel family inhibition at each step (Figure 4.1.1 B, B' and C). Total K current was defined using a high concentration of TEA together with all the Kv channel inhibitors at the end of the experiment.

Using this protocol, we found that in Aβ SA1-LTMRs and Aβ RA-LTMRs, Kv1 and Kv3 account for more than 80% of outward current during their APs (Figure 4.1.2 A, B, and E). These two Kv channel families also account for the majority of potassium current during the AP in proprioceptors (19 ± 5% from Kv1 and 40 ± 6% from Kv3, n=11). We compared the currents activated during the AP waveform with that activated by a step to +20 mV for 30ms, long enough to achieve maximal activation for each channel type. Interestingly, in Aβ SA1-LTMRs and Aβ RA-LTMRs, Kv2 channels underlie a major component (~60-70%) of outward current during 30ms step depolarizations to +20 mV but contribute almost no current during the AP (Figure 4.1.2 A', B' and E'), apparently because of the slow opening kinetics of Kv2 channels and the relatively narrow AP waveforms of Aβ-LTMR subtypes. On the other hand, in $MrgD^{+}$ nonpeptidergic nociceptors, which have wide AP waveforms, Kv2 channels contribute substantial current during both AP and step depolarization commands, along with Kv1 and Kv4 channels; Kv3 channels also contribute significant outward current during the AP (13% of the total; Figure 4.1.2 C, C' and E). Strikingly, in C-LTMRs, Kv4 channels are the primary

mediator (> 80%) of outward current during both step depolarization and the AP (Figure 4.1.2 D, D' and E), thus revealing a major difference compared to Aβ-LTMRs, where Kv4-mediated current is minor. Thus, considerably different combinations of current from the various Kv channel families underlie the outward currents of DRG neuron subtypes during both the APs and step depolarizations.

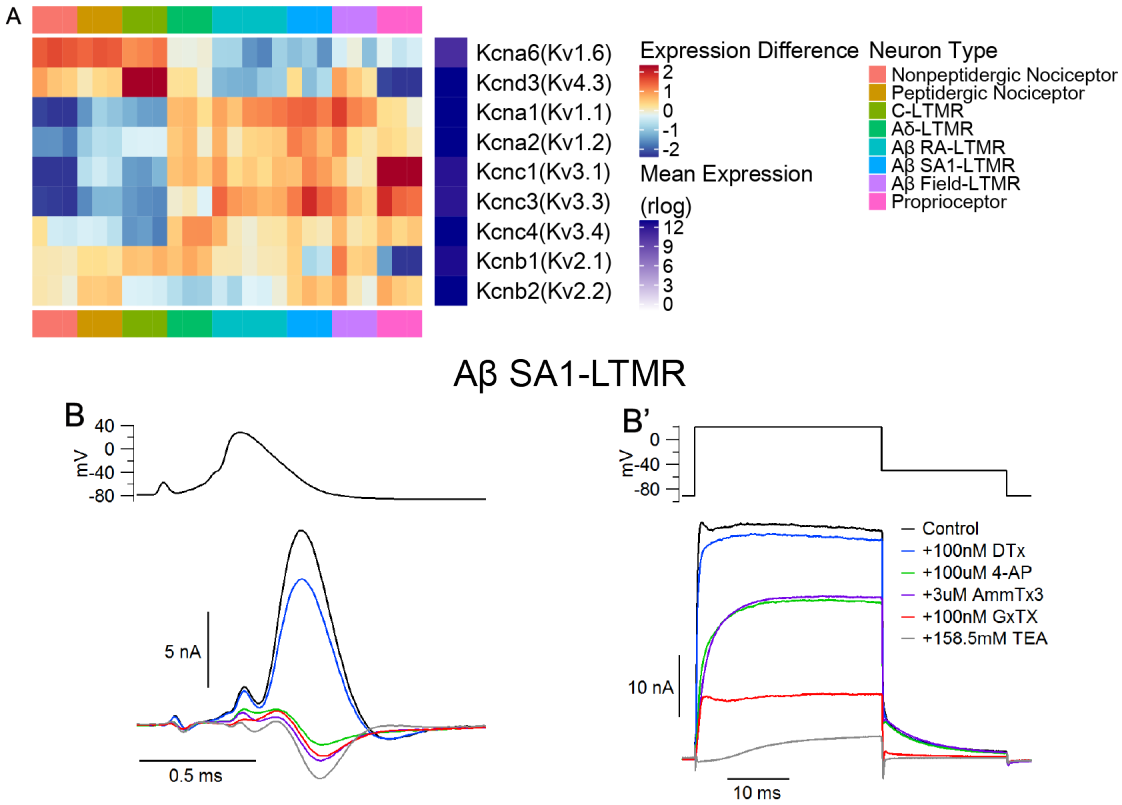

C

Agent	Target	IC50	Test Concentration
α-Dendrotoxin	Kv1.1, Kv1.2, Kv1.6	20 nM	100 nM
4-AP	Kv3	30 µM	100 µM
AmmTx3	Kv4.2, Kv4.3	100 nM	3 µM
Guangxitoxin-1E	Kv2.1, Kv2.2	5 nM	100 nM

Figure 4.1.1. Experimental strategies to examine subtype-specific contributions of Kv channel families to outward current.

(**A**) Heatmap depicting expression level differences of the most abundantly expressed Kv1, Kv2, Kv3 and Kv4 channel subunits. Expression deviation from the average expression level is plotted in the heatmap. Average expression level is plotted in the color gradient column next to the heatmap.

(**B**, **B'**) An example of an outward current recorded during voltage commands following stepwise applications of a series of channel inhibitors. Shown are example traces of outward currents recorded from an Aβ SA1-LTMR, during the AP waveform command (**A**) and a step depolarization (**A'**) without potassium channel inhibitors (black trace) and following step-wise application of a series inhibitors: DTX (blue trace), 4-AP (green trace), AmmTX3 (purple trace), GxTX (red trace) and TEA (grey trace). The series of inhibitors specifically inhibit Kv1, Kv3, Kv4, Kv2 and all K channels, respectively.

(**C**) Table showing Kv channel inhibitors and corresponding concentrations used in (**B**, **B'**) and Figure 4.1.2, and the major channel targets they inhibit.

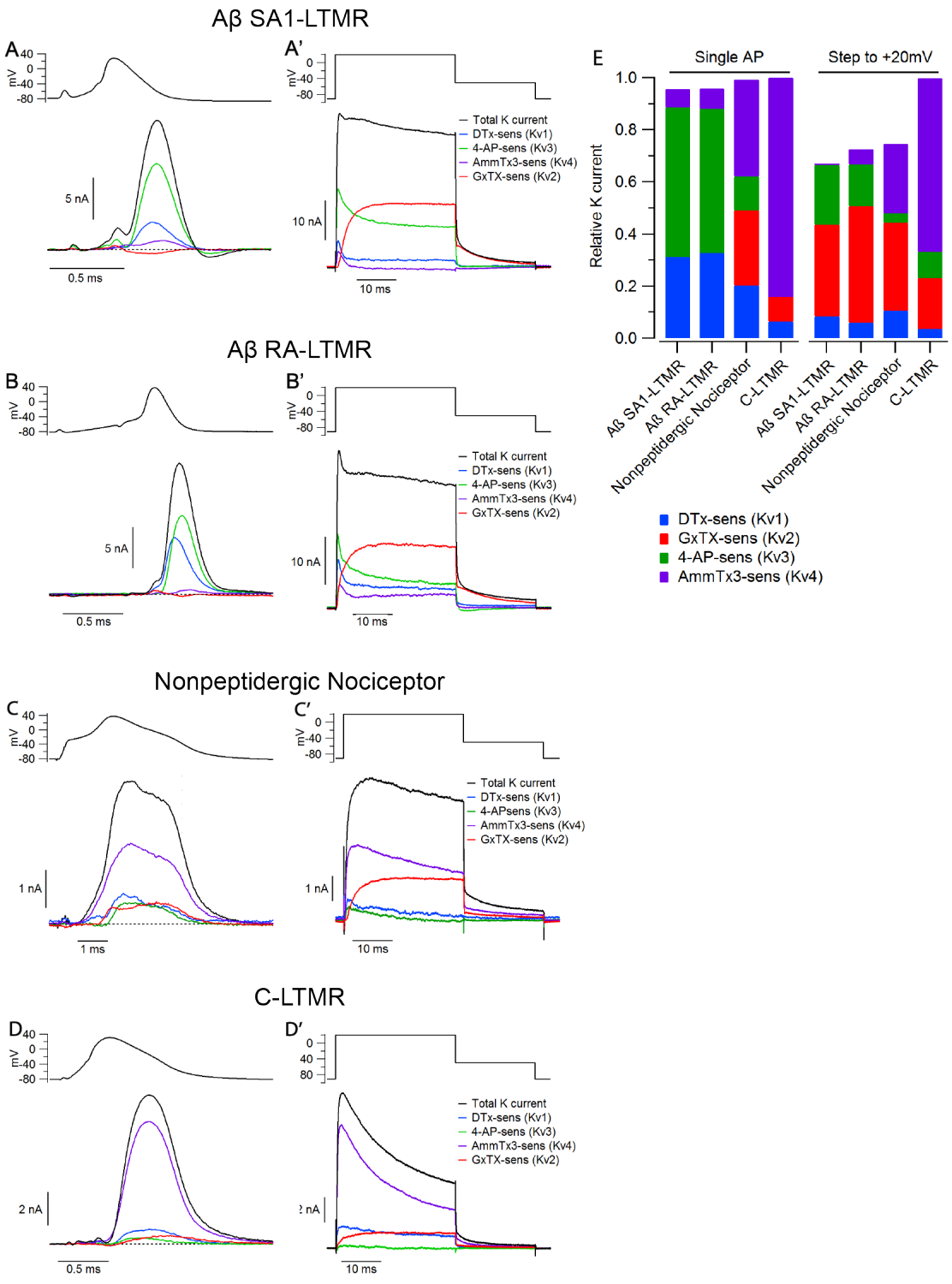
Aβ SA1-LTMR
A
A'
mV
5 nA
0.5 ms
10 nA
10 ms
Total K current
DTx-sens (Kv1)
4-AP-sens (Kv3)
AmmTx3-sens (Kv4)
GxTX-sens (Kv2)
Aβ RA-LTMR
B
B'
Nonpeptidergic Nociceptor
C
C'
1 nA
1 ms
C-LTMR
D
D'
2 nA
E
Single AP
Step to +20mV
Relative K current
Aß SA1-LTMR
Aß RA-LTMR
Nonpeptidergic Nociceptor
C-LTMR
DTx-sens (Kv1)
GxTX-sens (Kv2)
4-AP-sens (Kv3)
AmmTx3-sens (Kv4)

Figure 4.1.2. Kv channel families differentially contribute to outward current in DRG sensory neuron subtypes.

(**A-D**) Representative traces of components of Kv current during the AP of Aβ SA1-LTMRs (**A**), Aβ RA-LTMRs (**B**), $MrgD^+$ nonpeptidergic nociceptors (**C**), and C-LTMRs (**D**). Shown are representative traces of total outward K^+ currents (black), currents contributed by Kv1 (blue), Kv3 (green), Kv4 (purple) and Kv2 (red) under corresponding AP waveforms. Current was evoked by AP waveforms (previously recorded in a different cell of each type), and components of current were isolated by sequential cumulative application of 100 nM α-Dendrotoxin (DTX), 100 μM 4-aminopyridine (4-AP), 3 μM AmmTX3, and 100 nM Guanxitoxin-1E (GxTX) to identify Kv1, Kv3, Kv4 and Kv2 currents, respectively.

(**A'-D'**) Representative traces of outward currents measured during a step depolarization command in in Aβ SA1-LTMRs (**A'**), Aβ RA-LTMRs (**B'**), $MrgD^+$ nonpeptidergic nociceptors (**C**'), and C-LTMRs (**D'**). Currents were evoked by a step depolarization to +20 mV for 30 ms, applied in parallel with the AP commands in the same cells as **A**-**D**.

(**E**) Stacked bar plots showing the average fraction of total outward K+ current carried by Kv1, Kv2, Kv3, Kv4 channels in Aβ SA1-LTMRs (AP waveform: 31 ± 3% Kv1, 0 ± 1% Kv2, 59 ± 3% Kv3, 7 ± 1% Kv4; Step to +20 mV: 9 ± 2% Kv1, 35 ± 3% Kv2, 22 ± 3% Kv3, 1 ± 1% Kv4; n = 15), Aβ RA-LTMRs (AP waveform: 33 ± 4% Kv1, 0 ± 2% Kv2, 58 ± 4% Kv3, 8 ± 2% Kv4; Step to +20 mV: 6 ± 3% Kv1, 45 ± 8% Kv2, 16 ± 7% Kv3, 6 ± 3% Kv4; n = 11), $MrgD^+$ nonpeptidergic nociceptors (AP waveform: 20 ± 4% Kv1, 29

± 6% Kv2, 13 ± 3% Kv3, 37 ± 6% Kv4; Step to +20 mV: 11 ± 3% Kv1, 34 ± 7% Kv2, 4 ± 2% Kv3, 27 ± 4% Kv4; n = 11), and C-LTMRs (AP waveform: 7 ± 2% Kv1, 10 ± 1% Kv2, 0 ± 3% Kv3, 86 ± 3% Kv4; Step to +20 mV: 4 ± 2% Kv1, 19 ± 2% Kv2, 10 ± 2% Kv3, 67 ± 3% Kv4; n=11). Current contributions were quantified by integrating the currents during the AP or the 30 ms step depolarization.

4.2. Kv1 channels govern firing patterns in a subtype-specific manner

The differential expression and current contributions of voltage-gated potassium channel family members across DRG neuron subtypes suggest that they are critical for shaping subtype specific firing properties. In general, the functional role of any one kind of channel cannot be defined in isolation but depends on the context of the many other channels present (Goldman et al., 2001). We explored the effect of inhibiting Kv1 channels using the Kv1 blocker α-DTX. All the cell types expressed various Kv1 subunits, primarily Kv1.1, Kv1.2, and Kv1.6, with differing expression levels in the different cell types of each subunit, all of which are targeted by α-DTX. In Aβ SA1-LTMRs and Aβ Field-LTMRs, which both express high levels of Kv1.1 and Kv1.2, firing evoked by 500-ms current steps shows a strongly adapting firing pattern, firing only early in the depolarization. In both LTMR subtypes, blocking Kv1 channels with α-DTX dramatically converted their non-repetitive firing patterns to sustained repetitive firing lasting through the current injection (Figure 4.2.1 A-F). Aβ RA-LTMRs also express substantial Kv1.1 and Kv1.2 subunits but show sustained repetitive firing up to 200 Hz under control conditions. In these cells, α-DTX enhanced firing for small depolarizations but had little effect on firing rates for large current injections (Figure 4.2.1 G-I), in contrast to the dramatic enhancement of maximal firing seen in Aβ SA1-LTMRs and Aβ Field-LTMRs. In both $MrgD^+$ nonpeptidergic nociceptors and C-LTMRs, Kv1.6 is enriched, compared to medium/large-diameter neuron subtypes. These two subtypes of small-diameter neurons both responded to α-DTX application but in different ways, with α-DTX substantially increasing the maximal firing rate of $MrgD^+$ nonpeptidergic nociceptors which is relatively low (~10 Hz) in control conditions (Figure 4.2.1 J-L),

while having little effect on maximal firing rate of C-LTMRs (which in control fire up to ~28 Hz) but inducing an early cessation of firing and thus a rapid drop in spike number during large current injections (Figure 4.2.1 M-O). This effect may result from a more depolarized membrane potential during the trough between APs, facilitating inactivation of sodium channels. These findings show that inhibiting Kv1 currents has a wide range of effects on firing. The differing effects may reflect a combination of the levels of expression together with the different context of all the other channel types in the neurons as well as potentially different kinetic properties of Kv1 channels subunit compositions (including accessory subunits).

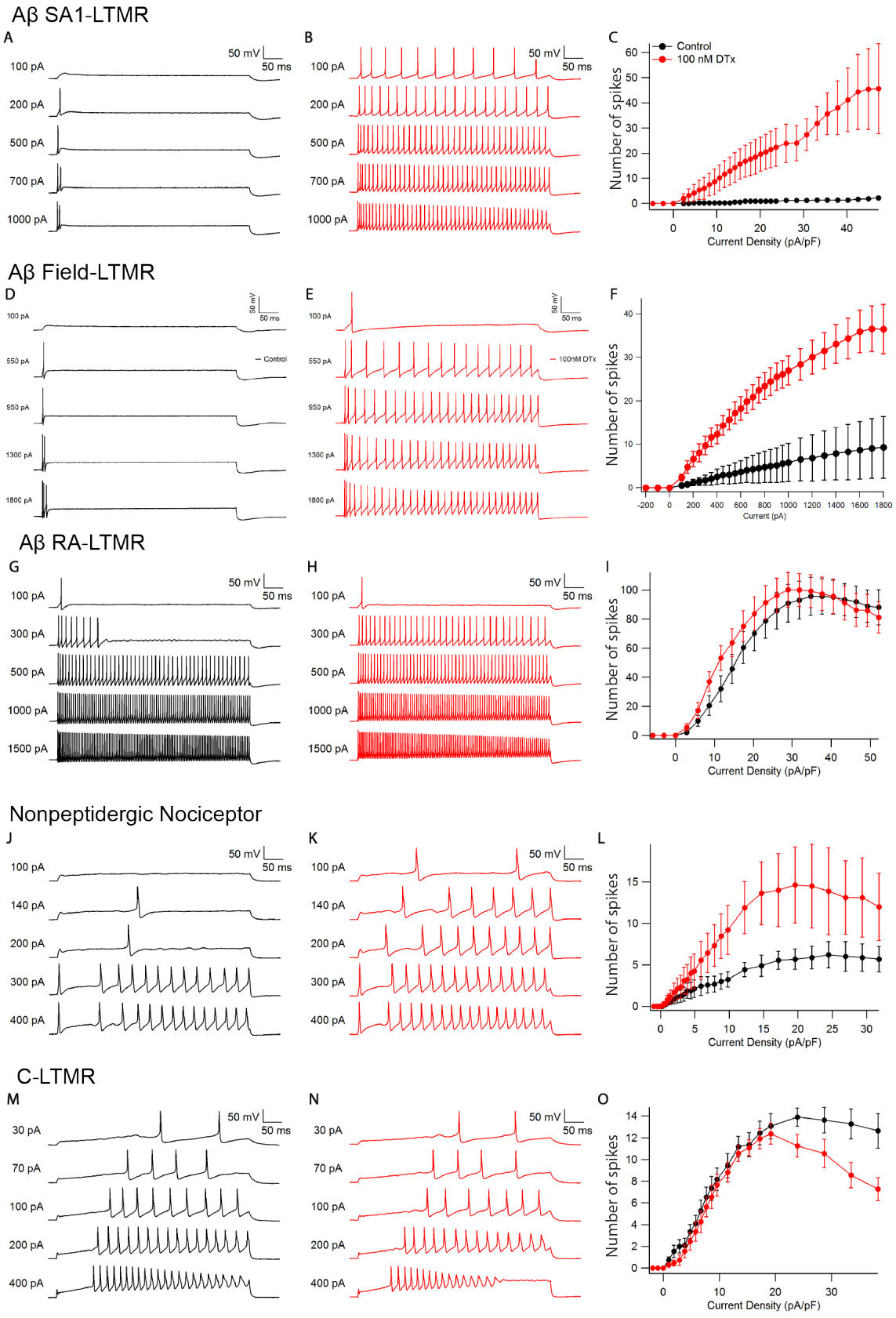
Aβ SA1-LTMR
A
50 mV
50 ms
100 pA
200 pA
500 pA
700 pA
1000 pA
B
50 mV
50 ms
100 pA
200 pA
500 pA
700 pA
1000 pA
C
Control
100 nM DTx
Number of spikes
Current Density (pA/pF)
Aβ Field-LTMR
D
50 mV
50 ms
100 pA
550 pA
Control
950 pA
1300 pA
1800 pA
E
50 mV
50 ms
100 pA
550 pA
100nM DTx
950 pA
1300 pA
1800 pA
F
Number of spikes
Current (pA)
Aβ RA-LTMR
G
50 mV
50 ms
100 pA
300 pA
500 pA
1000 pA
1500 pA
H
50 mV
50 ms
100 pA
300 pA
500 pA
1000 pA
1500 pA
I
Number of spikes
Current Density (pA/pF)
Nonpeptidergic Nociceptor
J
50 mV
50 ms
100 pA
140 pA
200 pA
300 pA
400 pA
K
50 mV
50 ms
100 pA
140 pA
200 pA
300 pA
400 pA
L
Number of spikes
Current Density (pA/pF)
C-LTMR
M
50 mV
50 ms
30 pA
70 pA
100 pA
200 pA
400 pA
N
50 mV
50 ms
30 pA
70 pA
100 pA
200 pA
400 pA
O
Number of spikes
Current Density (pA/pF)

Figure 4.2.1. Blocking Kv1 channels impacts DRG neurons' firing patterns in a subtype-specific manner

(**A**-**B**, **D**-**E**, **G**-**H**, **J**-**K**, **M**-**N**) Representative voltage traces showing spike patterns of an Aβ SA1-LTMR (**A**-**B**), Aβ Field-LTMR (**D**-**E**), Aβ RA-LTMR (**G**-**H**), $MrgD^+$ polymodal nociceptor (**J**-**K**), and C-LTMR (**M**-**N**) during 500-ms of sustained current injection before (**A**, **D**, **G**, **J**, **M**) and after (**B**, **E**, **H**, **K**, **N**) application of α-DTX.

(**C**, **F**, **I**, **L**, **O**) Number of spikes during 500-ms current injections are plotted against injected current density before (black curve) and after (red curve) α-DTX for Aβ SA1-LTMRs (**C**, n = 6), Aβ Field-LTMRs (**F**, n = 13), Aβ RA-LTMRs (**I**, n = 15), $MrgD^+$ nonpeptidergic nociceptors (**L**, n = 9), and C-LTMRs (**O**, n = 11). Data are represented as mean ± SEM.

4.3. Kv4.3 uniquely regulates the delayed firing pattern of C-LTMRs

In contrast to Aβ-LTMRs, Kv4 channels are the major source of K current in C-LTMRs. In addition, *in vivo* immunostaining showed that Kv4.3 is present on peripheral endings and likely at central terminals of C-LTMRs, suggesting a unique function of Kv4.3 in these neurons (Figure 4.3.1 A-B). Therefore, we next recorded C-LTMR firing patterns in the presence and absence of the Kv4 channel inhibitor AmmTx3. Interestingly, AmmTx3 application greatly reduced the long latency to the first AP following current injection, normally a distinguishing feature of C-LTMRs (Figure 4.3.2 A, B and D). Complementary experiments were performed using mice in which the *Kcnd3* (Kv4.3) gene was ablated (Figure 4.3.2 C, D). As with the pharmacology experiments, C-LTMRs with a targeted deletion of Kv4.3 exhibited a markedly reduced latency to the first AP, confirming that Kv4.3 is indeed essential for the delayed firing of C-LTMRs. Thus, as with Kv1 family members and Aβ-LTMR subtypes, Kv4.3, which is uniquely expressed in C-LTMRs and governs unique aspects of their intrinsic physiological properties.

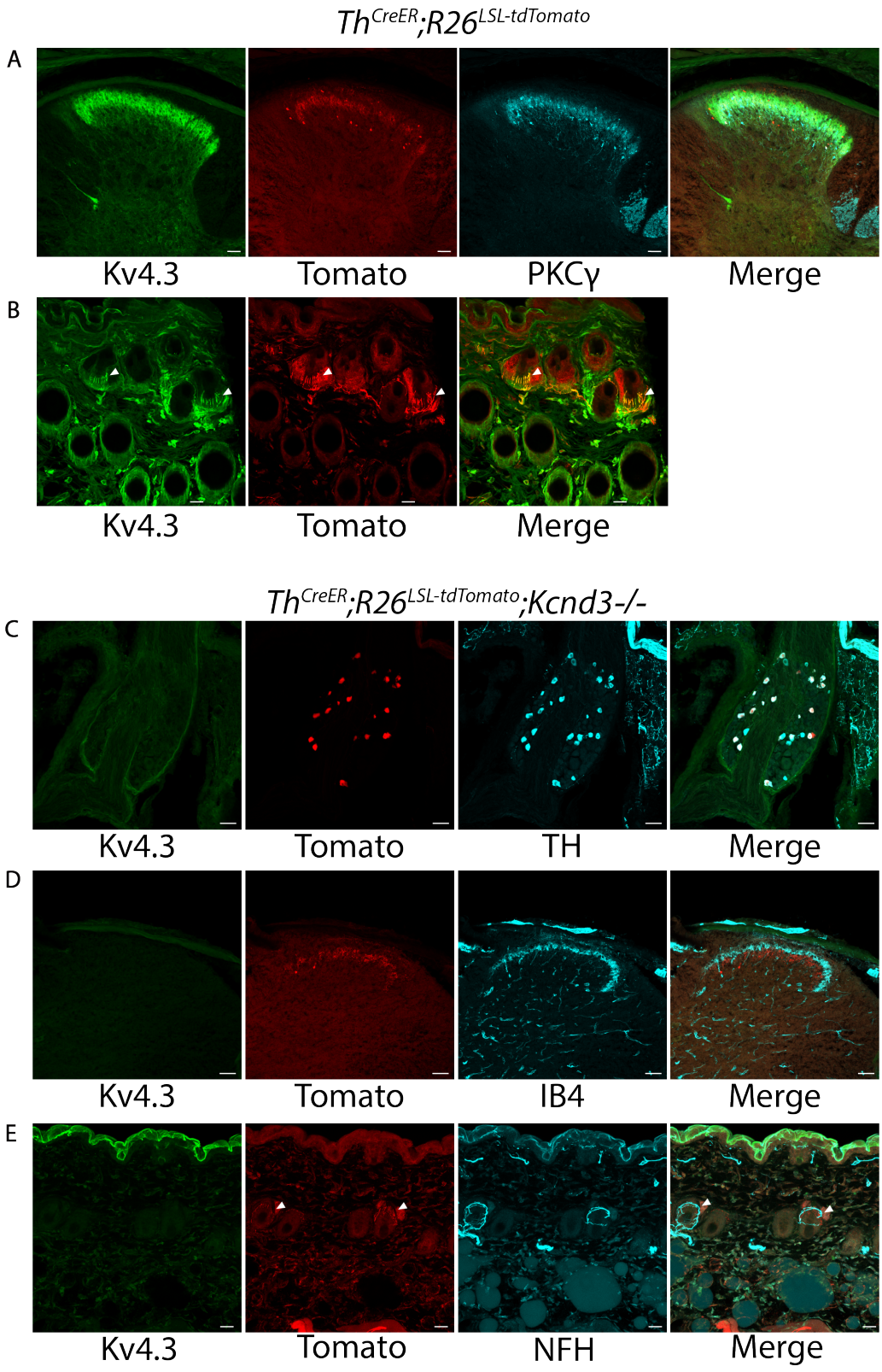
Th^CreER;R26^LSL-tdTomato
A
Kv4.3
Tomato
PKCγ
Merge
B
Kv4.3
Tomato
Merge
Th^CreER;R26^LSL-tdTomato;Kcnd3-/-
C
Kv4.3
Tomato
TH
Merge
D
Kv4.3
Tomato
IB4
Merge
E
Kv4.3
Tomato
NFH
Merge

Figure 4.3.1. Kv4.3 is present in C-LTMR axon terminals *in vivo*, and its deletion does not change the general morphology of C-LTMRs.

(**A**) Representative images of triple-immunostaining with Kv4.3, tdTomato, and PKCγ in cross sections of spinal cords from $Th^{2A\text{-}CreER}$; $R26^{lsl\text{-}tdTomato}$ mice (Tamoxifen 2 mg/day at P21-22). Kv4.3, tdTomato, PKCγ are shown in separate channels, and the merged channel image shows that Kv4.3 expression in the spinal cord dorsal horn largely overlaps with tdTomato and PKCγ. (n = 3 mice) Scale bars, 50 μm.

(**B**) Representative images of double-immunostaining with Kv4.3 and tdTomato in back hairy skin sections from $Th^{2A\text{-}CreER}$; $R26^{lsl\text{-}tdTomato}$ mice (Tamoxifen 2 mg/day at P21-22). Kv4.3 and tdTomato are shown in separate channels, and the merged image shows that Kv4.3 is present in C-LTMR hair follicle lanceolate endings marked by tdTomato. (n = 3 mice) Scale bar, 20 μm.

(**C**) Representative images of triple-immunostaining with Kv4.3, tdTomato, and TH in DRG sections from $Th^{2A\text{-}CreER}$; $R26^{lsl\text{-}tdTomato}$; *Kcnd3-/-* mice (Tamoxifen 2 mg/day at P21-22) (n = 3 mice). Immunostaining shows no Kv4.3 signal in DRGs of *Kcnd3-/-* mice, verifying the specificity of the Kv4.3 antibody.

(**D**) Representative images of triple-immunostaining with Kv4.3, tdTomato, and IB4 in cross sections of spinal cords from $Th^{2A\text{-}CreER}$; $R26^{lsl\text{-}tdTomato}$; *Kcnd3-/-* mice (Tamoxifen 2 mg/day at P21-22) (n = 3 mice). Kv4.3 signal is undetectable in spinal cords of *Kcnd3-/-*

mice. TdTomato signal in C-LTMR central terminals is largely restricted to the region immediately ventral to the IB4 layer of the spinal cord dorsal horn, as in WT mice.

(**E**) Representative images of triple-immunostaining with Kv4.3, tdTomato, and NFH in back hairy skin sections from *Th*$^{2A\text{-}CreER}$*; R26*$^{lsl\text{-}tdTomato}$; *Kcnd3-/-* mice (Tamoxifen 2 mg/day at P21-22). No Kv4.3 signal is detected in the skin of *Kcnd3-/-* mice. TdTomato signal is present in lanceolate endings in these mutants, as it is in control mice.

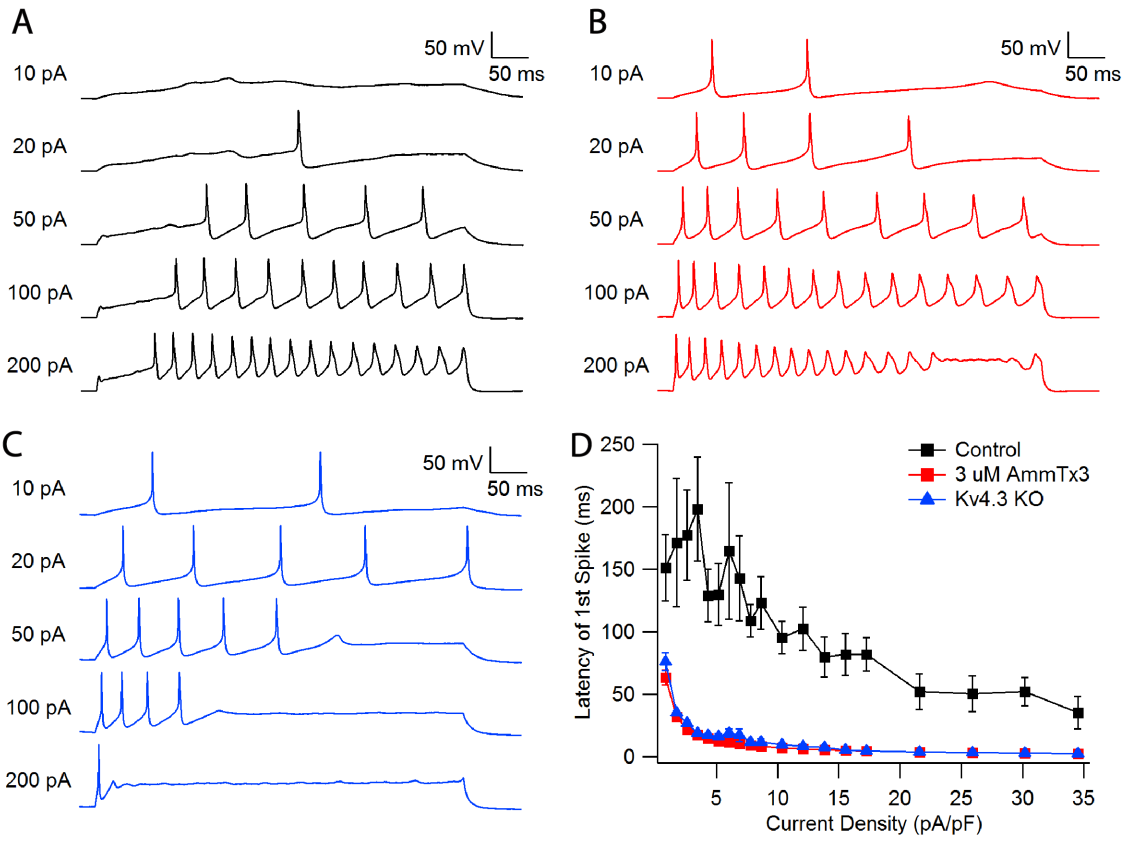

Figure 4.3.2. Kv4.3 underlies the delayed firing pattern of C-LTMRs.

(**A-B**) Representative voltage traces showing the spike patterns of the same C-LTMR during 500-ms of sustained current injection before (**A**) and after (**B**) exposure to the Kv4 channel inhibitor AmmTX3.

(**C**) Representative voltage traces showing the spike patterns of a C-LTMR from Kv4.3Δ mice during 500-ms of sustained current injection.

(**D**) Plot depicting latencies of the first spike as a function of injected current density for C-LTMRs, before (black curve), in C-LTMRs after (red curve) AmmTX3 application (n

= 8), and for C-LTMRs from Kv4.3Δ mice (blue curve) (n = 13). Latency was measured as the time from the beginning of the current injection to the peak of the first AP. Latencies are presented as mean ± SEM.

These pharmacological and genetic manipulation experiments support the notion that the unique combinations of Kv channels expressed in the eight DRG sensory neuron subtypes (summarized in Figure 5.1.1) are critical for subtype-specific intrinsic physiological properties.

CHAPTER 5: DISCUSSION

While it is well established that primary somatosensory neurons of the DRG are tuned to distinct stimuli and display unique firing patterns, the molecular machinery underlying their unique properties has remained largely elusive. Here, we used a combination of sensory neuron subtype-specific genetic labeling and deep RNA-sequencing to generate transcriptome profiles for each of eight major DRG neuron subtypes. Guided by these transcriptome data, we used *in vitro* electrophysiology with pharmacological and molecular-genetic tools to explore the molecular basis of sensory neuron subtype-specific electrical properties. These functional analyses demonstrated that our transcriptome data has predictive value for determining the roles of select ion channels in shaping subtype-specific intrinsic properties. Therefore, we propose a model in which the voltage-gated ion channels listed in Figure 5.1 are the key determinants of the characteristic intrinsic electrophysiological properties of each of the five LTMRs and other DRG sensory neuron subtypes.

The deep transcriptome analysis described here has unique value for assessing the contributions of genes, including those encoding ion channels, in a sensory neuron subtype-specific manner. While prior bulk sequencing or microarray studies using genetically labeled DRG neuron subtypes have been reported, these studies either used genetic tools targeting broad populations of DRG neurons rather than functionally or physiologically defined subsets or sequenced a limited number of subtypes (Chiu et al., 2014; Fleming and Luo, 2013). In addition, unsupervised single cell sequencing studies of DRG neurons did not resolve several key, functionally distinct neuronal subtypes,

notably the Aβ-LTMR subtypes (Li et al., 2016; Usoskin et al., 2015). This is likely due to the relatively small numbers of Aβ-LTMRs, similarities in their gene expression patterns, especially for Aβ SA1-LTMRs and Aβ Field-LTMRs, the small numbers of neurons sequenced in prior studies, and the potential difficulty maintaining the integrity of large diameter DRG neurons during isolation procedures. For guiding functional analyses, the transcriptome profiles generated in the present study cover eight major DRG neuron subtypes, including three Aβ-LTMR subtypes, Aδ-LTMRs and C-LTMRs, with high sequencing depth, and thus complement and extend findings from prior sequencing analyses. Indeed, the transcriptome profiles reported here reveal a large number of functionally relevant genes, including ion channels, and lowly expressed genes that are differentially expressed across DRG neuron subtypes, including Aβ-LTMR subtypes, providing a valuable resource for identifying molecular underpinnings of subtype-specific electrophysiological properties and functions. It is noteworthy that the transcriptome profiles also reveal genes useful for generating new genetic tools, as demonstrated for Calb1 (Figure 3.1.4). These profiles may also be useful for identifying pharmacological targets for treating disorders of somatosensation.

The transcriptome profiles revealed a particularly striking diversity of voltage-gated ion channels expressed among the neuronal subtypes. One of the most notable differences observed is for Nav channels. While Nav1.7 is broadly expressed among neuronal subtypes, with the exception of proprioceptors, the TTX-insensitive channels Nav1.8 and Nav1.9 are enriched in C-fiber subtypes, including C-LTMRs. The Aδ-LTMRs and three Aβ-LTMR subtypes as well as proprioceptors express both Nav1.1 and Nav1.6, which is

consistent with previous work that assessed the distribution of voltage-gated sodium channels in DRG neurons with different sizes (Dib-Hajj et al., 2010). Despite a recent study suggesting that Nav1.1 uniquely functions in myelinated nociceptors (Osteen et al., 2016), our findings implicate this channel, along with Nav1.6, as the major determinants of Nav currents in most and possibly all large-diameter DRG sensory neuron subtypes. This is particularly interesting when considering approaches to block excitability of large diameter sensory neuron types, including Aβ-LTMR subtypes for the prevention of tactile hypersensitivity and mechanical allodynia in neuropathic pain states. Future work will be required to assess the relative contributions of Nav1.1 and Nav1.6 in Aδ-LTMRs, Aβ RA-LTMRs, Aβ SA1-LTMRs and Aβ Field-LTMRs under both normal and disease conditions.

Towards our goal of defining the molecular basis of sensory neuron subtype-specific intrinsic membrane properties, we used the transcriptome findings to guide an analysis of the contributions of several families of Kv channels. We found that Kv1.1 and Kv1.2 are highly expressed in each of the Aβ-LTMRs where they generally suppress firing. Curiously, although Kv1 channels carry a large fraction of outward current in Aβ SA1-LTMRs and Aβ Field-LTMRs during the AP, and are critical for the non-repetitive firing patterns observed for the two LTMR subtypes, α-DTX sensitive Kv1 channels also mediates a large component of the outward current in Aβ RA-LTMRs, which exhibit robust, high-frequency repetitive firing in response to current injection. It is possible that the Kv1 channels in Aβ RA-LTMRs have different kinetics or voltage-dependence because of different tetrameric composition of α subunits, auxiliary subunits, or

posttranscriptional modifications, or it may be that the background of other conductances helps control repetitive versus non-repetitive firing patterns. It is also likely, as previous computational modeling has suggested, that the ratio of potassium and sodium currents is critical in determining repetitive versus non-repetitive firing patterns (Youssef et al., 2008). Thus, subtle differences in the ratios of Kv and Nav channel expression levels among the three Aβ-LTMR subtypes may underlie repetitive versus non-repetitive firing patterns.

The transcriptome data support additional predictions about the roles of channels that function in select sensory neuron subtypes. To test one of these predictions, we focused on Kv4.3 because it is highly and uniquely expressed in C-LTMRs. Our findings revealed that Kv4.3 indeed carries a majority of outward current in C-LTMRs, during both the AP and step depolarization. Moreover, this potassium channel contributes both to the wide AP waveform of C-LTMRs as well as its delayed firing property, which is a unique electrophysiological signature of C-LTMRs.

Our electrophysiological analysis focused on the firing patterns of DRG cell bodies. Of course, different cell regions almost certainly have different expression levels of the channels described herein (Trimmer, 2015). In future work it will be important to explore possible region-specific expression of the channels. In the case of Kv4.3 in C-LTMRs, immunohistochemical analysis showed that this channel is distributed throughout the entire cell surface of C-LTMRs, including its peripheral lanceolate endings around hair follicles and its central terminals in dorsal horn lamina II_{iv}. This subcellular localization

pattern is in contrast to brain neurons, in which Kv4.3 is highly polarized, with localization limited to dendrites, and in certain cells to cell bodies, but not on axons in any cell types investigated (Trimmer, 2015; Vacher et al., 2008). Considering that Kv4.3 operates within the subthreshold voltage range in C-LTMR peripheral terminals, it may mediate signal integration and govern AP initiation, which in turn may underlie the distinct responses to dynamic features of mechanical stimuli that have been noted for these neurons (Rudomin, 1999). First, a long mechanical stimulus contact time is required to induce spiking in C-LTMRs *in vivo*. This long inertia may be due to Kv4.3 activation at subthreshold voltages. The required long contact time may, in turn, account for the C-LTMR's signature speed tuning curve in response to stimuli moving across skin in humans. These neurons respond more vigorously to stroking the skin at slow speeds (1-10 cm/s in human, 1 mm/s in cat) (Löken et al., 2009; Rudomin, 1999). This responsiveness to a 'pleasurable' rate of skin stroking (Löken et al., 2009), which distinguishes C-LTMRs from other LTMRs, leads us to speculate that Kv4.3 underlies this unique tuning property, which is suggested to contribute to affective touch. Second, C-LTMRs cannot follow high oscillatory stimulations, which can be explained by the delayed firing resulting from Kv4.3 expression. Third, C-LTMRs respond to rapid cooling of the skin, but not slow cooling, and this too may reflect the kinetics of activation of Kv4.3. Finally, the dominance of Kv4.3 in the repolarization of the wide AP in C-LTMRs supports the additional prediction that this potassium channel governs the amount of neurotransmitter release in the dorsal horn.

In summary, deep sequencing of genetically labeled sensory neuron subtypes has afforded an opportunity to explore the molecular determinants of DRG sensory neuron subtype-specific intrinsic physiological properties. Our pharmacological and genetic dissection of a subset of potassium channels reveals unique roles of channel families in shaping AP properties and firing patterns. The findings lend support to the notion that the deep sequencing measurements are highly predictive of ion channel contributions to the remarkably unique physiological properties of DRG sensory neuron subtypes. We propose that the voltage-gated ion channels listed in Figure 5.1.1 are the principal molecular determinants of unique intrinsic electrophysiological properties of the five LTMR subtypes, peptidergic and $MrgD^{+}$ nonpeptidergic polymodal nociceptors, and proprioceptors, and thereby underlie their distinct functions in somatosensation.

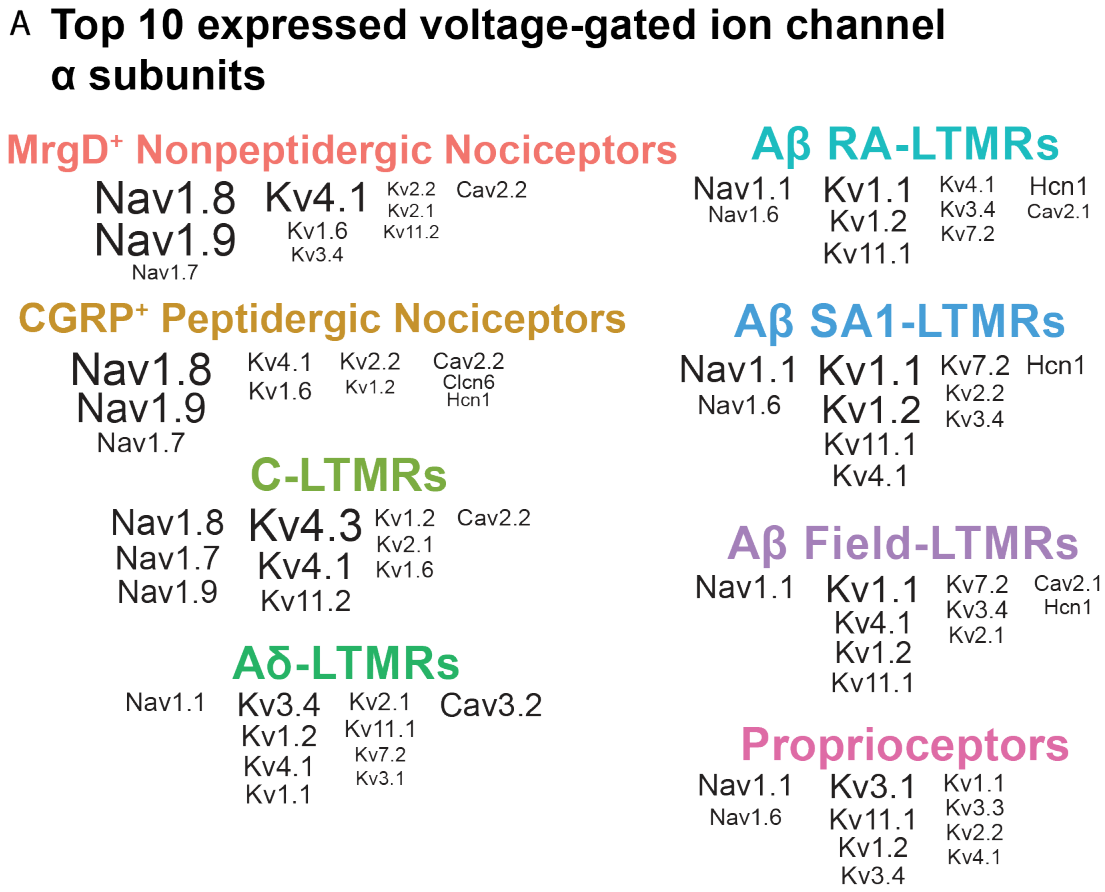

Figure 5.1.1. Most highly expressed voltage-gated ion channel α subunits in each DRG somatosensory neuron subtype.

(**A**) Summary plot showing the ten most highly expressed voltage-gated ion channel α subunits in each sensory neuron subtype, ranked by rpkm value. The font size of the channel name corresponds to the relative rpkm expression value, but maxed out at rpkm = 150.

EXPERIMENTAL PROCEDURES

Tamoxifen treatments

Tamoxifen was dissolved in ethanol (20 mg/ml), which was stored at -20°C, then mixed with double volume of sun flower seed oil (Sigma), vortexed for 5-10 mins and centrifuged under vacuum for 20-30 min to remove the ethanol. The working solution (10 mg/ml) was kept at -20 ºC and delivered via oral gavage. For all analyses, the morning after coitus was designated as E0.5 and the day of birth as P0. For labeling C-LTMRs, 2mg/ml was injected at either P13-14 or P21-22 were used. The latter was used for *Th*$^{2A\text{-}CreER}$*; R26*$^{lsl\text{-}tdTomato}$*; Kcnd3-/-* mice after weaning, so that parents avoided exposure to tamoxifen. Labeling specificity at both time windows is high. For labeling Aδ-LTMRs, tamoxifen was given to *TrkB*^{CreER}*; R26*$^{lsl\text{-}tdTomato}$ mice at E12.5-14.5 to reduce glial cell labeling, which was critical for FACS sorting. For labeling Aβ SA1-LTMRs, tamoxifen was given to *TrkB*^{CreER}*; R26*$^{lsl\text{-}tdTomato}$ mice at E12.5-14.5 to reduce glial cell labeling. For labeling Aβ SA1-LTMRs, tamoxifen was given to *TrkC*^{CreER}*; Ret*^{fGFP} at E12.5 before 12PM; tamoxifen delivery at a later time point may increase off-target labeling.

In vitro current-clamp and voltage-clamp experiments

Preparation of DRG neurons. Dissociated DRG neurons were prepared using enzymatic treatment as previously described (Liu et al., 2017). Briefly, DRG neurons were removed from mice (> P21), cut in half and treated for 20 minutes at 37 °C with 20 U/ml papain (Worthington Biochemical, Lakewood, NJ) and 5 mM DL-cysteine in a calcium- and magnesium-free (CMF) Hank's buffer containing 137 mM NaCl, 5.36 mM KCl, 0.33 mM Na2HP4, 0.44 mM KH2PO4, 5 mM HEPES, 5.55 mM glucose, 0.001% phenol red,

pH 7.40 adjusted with NaOH; 300~310 mOsm. Ganglia were then treated for 20 minutes at 37 °C with 3 mg/ml collagenase (type I; Roche Diagnostics, Indianapolis, IN) and 4 mg/ml dispase II (Roche Diagnostics) in CMF Hank's buffer. Cells were dispersed by trituration with a fire-polished glass Pasteur pipette in a solution composed of two media combined in a 1:1 ratio: Leibovitz's L-15 medium (Invitrogen, Grand Island, NY) supplemented with 5 mM HEPES, and DMEM/F12 medium (Invitrogen); this solution also had added 100 ng/ml nerve growth factor (NGF) (Invitrogen). Cells were then plated on glass coverslips treated with 40 μg/ml poly-D-lysine and then 20 μg/ml laminin (Invitrogen). Then cells were incubated at 37°C (5% CO2) for 3 hours, after which Neurobasal medium (Invitrogen) containing B-27 supplement (Invitrogen), penicillin and streptomycin (Sigma, St. Louis, MO), and 100 ng/ml NGF was added to the petri dish. Cells were stored at 4°C and used within 48 hours. DRG neurons with specific molecular markers were chosen for following electrophysiological recordings.

Electrophysiology. Recordings were performed at 37 °C using an Axon Instruments Multiclamp 700B Amplifier (Molecular Devices). Voltage or current commands were delivered and signals were recorded using a Digidata 1321A data acquisition system (Molecular Devices) controlled by pCLAMP 9.2 software (Molecular Devices). Electrodes were pulled on a Sutter P-97 puller (Sutter Instruments) and shanks were wrapped with Parafilm (American National Can Company) to allow optimal series resistance compensation without oscillation. The resistances of the pipettes were 2-4 MΩ. Seals were formed in Tyrode's solution consisting of 155 mM NaCl, 3.5 mM KCl, 1.5 mM CaCl2, 1 mM MgCl2, 10 mM HEPES, 10 mM glucose, pH 7.4 adjusted with NaOH. After establishing whole-cell recording, cell capacitance was nulled and series resistance

was partially (70-85%) compensated. The cell was then lifted and placed in front of a series of quartz fiber flow pipes attached with cyanoacrylate glue to a rectangular aluminum rod (cross section 1.5 cm × 0.5 cm) whose temperature was controlled to 38°C using resistive heating elements and a feedback-controlled temperature controller (TC-344B, Warner Instruments). The end of the rod as well as the flow pipes (extending 1 mm from the end of the rod) were lowered just to the surface of the bulk chamber solution, which was locally quickly warmed by the rod; with the temperature of the aluminum rod set to 38°C, the solution exiting from the flow pipes was measured at 37°C (Carter and Bean, 2009). All flow pipes are heated identically and continuously, allowing rapid solution changes without fluctuations of temperature. Solutions were changed (in ~ 1 second) by moving the cell from one pipe to another.

Solutions. The standard recording solutions had quasi-physiological ionic composition, with an internal solution consisting of 140 mM K aspartate, 13.5 mM NaCl, 1.6 mM MgCl2, 0.09 mM EGTA, 9 mM HEPES, 14 mM creatine phosphate (Tris salt), 4 mM MgATP, 0.3 mMTris-GTP, pH 7.2 adjusted with KOH and an external Tyrode's solution consisting of 155 mM NaCl, 3.5 mM KCl, 1.5 mM CaCl2, 1 mM MgCl2, 10 mM HEPES, 10 mM glucose, pH 7.4 adjusted with NaOH.

Sequence of inhibitors for dissecting K current components. The inhibitors were applied cumulatively in a sequence designed to maximize the effective selectivity for identifying each component of K current by applying imperfectly-selective inhibitors after the main off-target channels had already been inhibited. The K channel inhibitors were applied on a background of TTX (1 μM) and A-803467 (1 μM) to inhibit Na channels. First, α-dendrotoxin (Alomone Labs), which is highly selective for Kv1.1, Kv1.2, and Kv1.6

channels (Harvey and Robertson, 2004), was applied to 100 nM. Next, 4-aminopyridine (4-AP) (Sigma) was applied at 100 μM, a concentration at which it should inhibit Kv3 channels almost completely while having minimal effects on other channels except Kv1, which was already blocked (Coetzee et al., 1999; Gutman, 2005). Next the Kv4 inhibitor AmmTX3 (Smartox Biotechnology) (Maffie et al., 2013; Pathak et al., 2016) was applied at 3 μM, followed by the Kv2 inhibitor Guanxitoxin-1E (Peptide Institute) at 100 nM (Liu and Bean, 2014). Finally, a high concentration of TEA was applied (in the continuing presence of the other inhibitors) to inhibit any remaining K current, with the exception of the experiments with proprioceptors, using a solution in which TEA replaced both Na and K (158.5 mM TEACl, 1.5 mM CaCl2, 1 mM MgCl2, 10 mM HEPES, 10 mM glucose, pH 7.4 adjusted with TEAOH); block by this solution relative to control was considered to comprise the total K current.

In vitro mechanoclamp experiments

Preparation of DRG neuron culutre. Digestion solution, which contained 5 mg/mL dispase (Gibco Invitrogen,17105-041), 2 mg/mL collagenase (Type I, Worthington, LS004196) and 0.1 mg/mL DNase (Sigma, DN25) in HBSS, was aliquoted and stored in -80 ºC. DH10 solution was made with 1×Penicillin-Streptomycin (Pen-Strep) (Life Technologies, 15070-063), 10% SCG FBS (Life Technologies, 16000-044, thawed and heat-inactivated in 55 ºC water bath for 30 minutes, aliquoted and stored in -20 ºC) in DMEM (high glucose DMEM, Life Technologies, 11965-118), filtered through 0.2 μm filters, and stored in 4 ºC for up to a month. Poly-D-lysine coated glass bottom petri dishes (MatTek, P35GC-1.5-10-C) were coated with 200 μL laminin (10 μg/mL) (Life

Technologies, 23017-015), incubated at 37 ºC overnight. The petri dishes were rinsed with ddH_2O three times and dried in a sterile fume hood.

DRGs were freshly dissected out from mice (3-16 weeks) and placed into ice-cold DH10, briefly washed once in 1×HBSS, then digested in 1 mL digestion solution at 37ºC for 30-40 minutes under constant rotation, and then centrifuged at 200 g for 5 minutes. The supernatant was removed while the precipitant was carefully resuspended in 1 mL DH10. Resuspended cells were gently triturated for 10-15 times using a pipette tip opening diameter no smaller than 0.5 mm, then allowed to recover for 1-2 minutes before the supernatant was collected and plated on glass areas in the dishes. Petri dishes were incubated in 37 ºC humidified atmosphere (5% CO_2) for 20 minutes, then ~2 mL pre-warmed DH10 medium together with 25 ng/mL nerve growth factor (NGF), 25 ng/mL brain-derived neurotrophic factor (BDNF), 25 ng/mL neurotrophin (NT3) and 2 ng/mL glia-derived neurotrophic factor (GDNF) was added. Neurons were kept in the incubator overnight.

In vitro mechanoclamp. The method for *in vitro* mechanoclamp experiments was modified from that of Hao and Delmas, 2011. Mechanical probes and patch pipettes were fabricated from borosilicate glass tubing (Sutter, BF150-86-10). Pipettes were pulled on a P-97 pipette puller (Sutter) and fire-polished using a De Fonbrune microfuge. Mechanical probes were polished to obtain a blunt tip that had a diameter of 3-4 μm. Patch pipettes has a resistance of 2~4 MΩ.

For mechanical stimulation, a piezoelectric actuator (P-601.1S, Physik Instrument) was fixed on a micromanipulator and a pipette holder was mounted on the actuator. The mechanical probe was positioned at an angle 45-60° from the horizontal plane.

Movement of the mechanical probe was controlled and monitored using the pCLAMP program. A step protocol was used to deliver mechanical stimulations with increasing displacements at 1μm increments. The probe moved at a speed of 500 μm/s (measured between 10%-90% distance) and displacement lasted for 500ms, followed by a 20 ms interval before the next stimulation. The zero position was found as follows: first, the probe tip was moved close to the cell under visual guidance; then a protocol with 4,5,6 μm stimulations was run. When the 4 μm stimulation did not yield any membrane deformation while 6 μm movement yielded visible membrane deformation, the zero position was defined as the -5 μm position.

Solutions. Internal solutions contained 125 mM CsCl, 1 mM $MgCl_2$, 4.8 mM $CaCl_2$, 10 mM HEPES, 10 mM EGTA, 4 mM Mg-ATP and 0.4 mM Na-GTP with pH adjusted with CsOH to 7.4, osmolarity adjusted to 300 mOsm with CsCl. Extracellular solutions contained 132mM NaCl, 3mM KCl, 1mM $MgCl_2$, 2.5mM $CaCl_2$, 10 mM HEPES and 10 mM glucose with pH adjusted with CsOH to 7.4, osmolarity adjusted to 300 mOsm with CsCl.

Fluorescence-activated cell sorting (FACS)

For preparation, three solutions were made beforehand. Digestion solution and DH10 medium were prepared and stored as described for the cell culture and *in vitro* mechanoclamp procedures. FACS solution included 50 mg/mL bovine serum albumin (BSA) (Sigma, A6003), 1 M HEPES (Sigma, H3375), 1×Pen-Strep, 0.5 mg/mL DNase in L-15 medium (Gibco, 11415). FACS solution was made fresh for every FACS experiment. For tissue collection, DRGs from all axial levels (except for proprioceptor

samples, for which only DRGs from thoracic levels were used, because it is known that $PV^{ires\text{-}Cre};R26^{lsl\text{-}tdTomato}$)were freshly dissected from mice (3-16 weeks of age) and placed into ice-cold DH10 with roots carefully removed, briefly washed once in 1×HBSS, then digested in 1mL digestion solution at 37 ºC under constant rotation. DRGs from up to six animals were collected for each FACS experiment and the total dissection time was kept under three hours. The digestant was centrifuged at 200 g for 5 minutes. The supernatant was removed while the precipitant was carefully resuspended in 1 mL DH10. Resuspended solutions were gently triturated 10-15 times using a pipette tip opening diameter no smaller than 0.5 mm, rested for 1-2 minutes before supernatants were collected to a new tube and then the precipitants underwent the same process of trituration, rest and collection of supernatants for a second time. Collected supernatants were passed through a 100 μm cell strainer (pre-rinsed with DH10) (Fisher, 08-771-19) followed by 2-3 mL DH10, and all solutions were collected and centrifuged at 200-300 g for 5 minutes. Supernatants were removed, and precipitants were gently resuspended in 8 mL DH10, centrifuged again and the pellets were resuspended in 1 mL FACS solution. The samples were immediately transported to a flow-cytometry facility on ice. MoFlo (Johns Hopkins School of Medicine) and Avalon (Harvard Medical School) sorters with 100 μm or 150 μm nozzles were used to sort fluorescent cells under pressure lower than ~20 psi. Sorting criteria were selected monitoring distribution of GFP and tdTomato signals, forward scatter, side scatter and pulse widths. Propidium iodide (PI) staining was sometimes used to exclude dead cells. A small portion of sorted cells was collected on a slide or culture medium for confirmation of fluorescence. Sorted cells used for RNA extraction were collected in RNAlater solution (Life Technologies, AM7022),

centrifuged, placed in 4 ºC overnight and sometimes stored in -80ºC for several days. RNA was purified using the Absolutely RNA nanoprep kit (Agilent, 400753).

RNA sequencing

Purified RNA samples with a concentration of ~1-10 ng/μL for 8-10μL (minimum total RNA > 1 ng) and RNA integrity number (RIN) above 7 (except for one sample for Aβ SA1-LTMRs that had an RIN ~ 6) were selected for library preparation and RNA-sequencing at the Johns Hopkins Deep Sequencing & Microarray Core. cDNA libraries were prepared using Nugen Ovation RNA-Seq and then Illumina TruSeq RNA Library Prep Kit. The cDNA libraries were then sequenced using the Illumina Hi-Seq 2000 platform with 50 bp single-end reads with 2× multiplexing (two samples were combined and run for each lane).

Trimethoprim treatment and characterization of *Calb1^{dgCre}* mice

Trimethoprim (TMP) (Sigma, T78883) was dissolved in DMSO (50mg/ml) and prepared fresh for intraperitoneal injection of mice carrying *Calb1^{dgCre}*. Mice were treated with two doses of TMP (100μg per gram of body weight per day at P18,19) and then sacrificed at P21-P28 for tissue harvesting (Sando et al., 2013). *Calb1^{dgCre}; R26$^{LSL-FSF-tdTomato}$* or *Calb1^{dgCre}; R26$^{LSL-FSF-tdTomato}$* mice display low level of baseline recombination. TMP treatment induced ~10-20 fold increase in the number of tdTomato^{+} cells in DRGs (data not shown). Variable baseline Cre activity was observed when using *Brn3a^{CKOAP}* as the reporter line (data not shown), and it is recommended that littermate controls be used to monitor baseline reporter expression or Cre activity.

Immunohistochemistry of cryosections

Mice (3-6 weeks) were anesthetized with CO_2 and perfused using 5-10 ml PBS followed by 10-20 ml of 4% paraformaldehyde (PFA) in PBS at room temperature (RT). Vertebral columns (including spinal cords and DRG) and skin were dissected from perfused mice. For immunostaining experiments other than those for Kv4.3, neuronal tissues were post-fixed in 4% PFA at 4ºC for 2-4 hours, while skin was post-fixed in Zamboni's fixation buffer at 4 ºC for 48 hours. For Kv4.3 immunostaining, no post-fixation was used for vertebral columns. For co-staining of Kv4.3 and tdTomato (related to Figure S7), the skin was post-fixed in Zamboni's fixation buffer at 4 ºC for one hour. In general, the tdTomato signal decreased as fixation times shortened, while the staining background increased as fixation times increased. Using one hour post-fixation, both signals could be observed, although the tdTomato signal was weak. Tissues were then washed 3×20 minutes with PBS at RT. Tissues were cryoprotected in 30% sucrose in PBS at 4 ºC overnight, embedded in OCT and frozen at -20 ºC, stored at -20 ºC for short term and -80 ºC for long term, and sectioned at 20-25μm using a cryostat. Sections were collected on slides and outlined using an ImmEdge Hydrophobic Barrier Pen. Vertebral column sections were dried at RT for at least 30 minutes or overnight before staining. Skin sections were dried at RT overnight to 48 hours. Slides were washed 3×10 min with PBS containing 0.1% Triton X-100 (0.1% PBST) and then blocked in 0.1% PBST containing 10% normal goat serum (Vector Labs, S-1000) or normal donkey serum (Jackson Immuno, 005-000-121) for 30min at RT. Slides were incubated with primary antibodies (listed in Key Resources Table) diluted in 0.1% PBST containing 5% serum at 4ºC overnight covered with parafilm (Fisher, PM996). The next day, Slides were washed

3x10 minutes with 0.1% PBST, and incubated with secondary antibodies diluted (species-specific Alexa Fluor 488, 546, and 647 conjugated IgGs, Invitrogen) 1:500 in 0.1% PBST containing 5% serum at room temperature for 2 hours, washed again 3×10 minutes with 0.1% PBST, and mounted with fluoromount-G (Southern Biotech).

Double fluorescent *in situ* hybridization (FISH) of cryosections

Digoxygenin (DIG) (DIG RNA labeling mix, Roche,11277073910)-labeled sense and antisense probes were generated for Lpar3, Adcyap1, Gpx3, Ptgfr, Spp1, and Fluorescein (Fluorescein RNA labeling mix, Roche, 11685619910)-labeled sense and antisense probes were generated for tdTomato and GFP. Five probes for each target gene were generated and tested using single-color *in situ* hybridization, and only probes that displayed robust signals were selected for subsequent analyses. For experiments, multiple solutions were prepared beforehand. Diethyl pyrocarbonate (DEPC)-ddH_2O and DEPC-PBS are ddH_2O and PBS treated with DEPC (Sigma, D5758) at 1:1000 ratio, mixed at 37 ^oC for at least 1 hour, then autoclaved. Washing buffer was 100 mM Tris-HCL, 150 mM NaCl, 0.05% Tween-20, pH 7.5 at 20 ^oC. Detection buffer was 100 mM Tris-HCL, 100 mM NaCl, 10 mM $MgCl_2$, and pH 8.0 at 20 ^oC. All the solutions were made in advance and stored in RT. Hybridization solution contained 50% formamide, 5× SSC, 0.3 mg/ml yeast tRNA (Sigma, R6750), 100 μg/ml heparin (Sigma, H3393), 1×Denhardt's (Sigma, D2532), 0.1% Tween 20, 5 mM EDTA in DEPC-ddH_2O. Hybridization solution was made in advance and stored at -20 ^oC. Vertebral columns were freshly dissected from mice (3-6 weeks) and frozen in OCT, then sectioned at 20-25 μm using a cryostat. Sections from at least one pair of cervical, thoracic, and lumbar DRGs were sectioned

and sections were collected on slides and warmed up at RT for 30 minutes. Sections were fixed in 4% PFA, then washed using freshly prepared DEPC in DEPC-PBS (1/1000) for 10 minutes and washed again with DEPC-PBS for 5 minutes. Slides were incubated in 50 μg/ml proteinase K for 1 to 5 minutes, then washed in DEPC-PBS for 5 minutes and rinsed with DEPC-ddH_2O (ddH_2O pretreated with DEPC, and autoclaved). Slides were treated with freshly made 0.1 M TEA buffer (triethanolamine and acetic anhydride in DEPC-ddH_2O) for 10 minutes at RT, then washed with DEPC-PBS for 5 minutes. Slides were then incubated in hybridization buffer and covered with parafilm and incubated at 65 ºC in a humidified chamber for 30 minutes, then in hybridization buffer with probes (1 DIG- and 1 fluorescein-labeled) diluted at 1:100 ratio at 65 ºC overnight. On the second day, slides were washed with 0.2×SSC once for 15 minutes at 65 ºC, then twice for 30 minutes each at 65 ºC. Slides were then incubated with 20% normal goat serum in 0.1% PBST for 30 minutes to an hour at RT, then added with AP labeled antibody (anti-DIG-AP, Roche, 11093274910) diluted at 1:1000-1:2000 in 20% normal goat serum in 0.1% PBST and incubated at RT for 2 hours, then washed 3×10 minutes in PBS or washing buffer. HNPP/Fast Red TR mix was prepared fresh, diluting 10 μL HNPP and 10 μL Fast Red TR stock solution in 1mL detection buffer (HNPP fluorescent detection kit, Roche, 11758888001), then filtered with 0.2 μm filter. Slides were then incubated in HNPP/Fast Red TR mix for 30 minutes at RT, and then washed in washing buffer. Next, slides were incubated in HNPP/Fast Red TR mix and washed repetitively for 3 times, then washed in PBS for 5 minutes, blocked with 0.5% blocking solution (blocking reagent (Roche, 11096176001) diluted in PBS) for 1 hour at RT, and then incubated in POD labeled antibody (anti-fluorescein-POD, Roche, 11426346910) (1:250 diluted in blocking

solution). Slides were washed in PBS 3×10 minutes at RT, then incubated with TSA Plus Solution (TSA diluted in Amplification Plus Buffer at 1:100) (TSA plus fluorescein system, PekinElmer NEL741001KT) for 15-30 minutes at RT, then rinsed again with PBS. Sections were mounted with fluoromount-G before being examined using confocal microscopy.

Data Analyses and Statistical Analyses

In vitro electrophysiology. Current and voltage records were filtered at 10 kHz and digitized at 200 kHz. Analysis was performed with Igor Pro 6.12 (Wavemetrics, Lake Oswego, OR), using DataAccess (Bruxton Software) to import pClamp data. Reported membrane potentials are corrected for a liquid junction potential of -10 mV between the internal solution and the Tyrode's solution in which current was zeroed before sealing onto the cell, measured using a flowing 3 M KCl reference electrode as described by Neher (1992). Voltage-clamp current records were corrected for linear capacitative and leak current by subtracting scaled responses to 5 mV hyperpolarizations delivered from the holding potential. In AP clamp experiments, APs were evoked by current injection (just above threshold for 0.5 ms) and then used as the command waveform in voltage clamp. To measure total net outward current during the repolarization phase of the AP, the current was integrated from the time that net current under control conditions became net outward (near the peak of the AP) to the time of the trough following the AP, when net current under control conditions shifted from outward to inward. Data are given as mean ± SEM and statistical significance was assessed using a two-tailed Student's T-test, paired or unpaired as appropriate.

In vitro mechanoclamp. Series resistance and junction potential were not compensated or corrected. Access resistance was assessed using membrane test with 5 mV hyperpolarizations from the holding potential throughout recordings, and cells display significant access time constant change were eliminated from further analysis. Kinetics of mechanosensitive currents were analyzed using pClamp and determined by using nonlinear least-squares regression analysis applied to the decay phase of the currents. We usually fit traces with one or two exponential components as follows: $I(t) = A_1 \cdot \exp(-t/\tau_1) + A_1 \cdot \exp(-t/\tau_1) + A_o$. Faster component τ was used in Figure 2.1.3. Only traces with a fitting correlation over 80% were selected.

RNA-sequencing. Reads were aligned and counted using STAR aligner and Htseq at Harvard Chan Bioinformatics Core. Both read count matrix and normalized data using reads per kilobase per million reads (rpkm) were obtained. Sequencing data quality was assessed by examining the number of mapped reads (average = 73,506,450), genomic mapping rate (average = 0.93), number of genes detected (19,601 genes that have a count number $\geqslant$ 1, 12,226 genes that have a count per million (CPM) value $\geqslant$ 1, 11,160 genes that have fpkm value $\geqslant$ 1), exonic mapping rate (average = 0.67), and rRNA mapping rate (average = 1.86×10^{-6}). Count matrix values were transformed using regularized log transformation implemented in DESeq2 R package and rendered homoscedastic (Love et al., 2014). Correlations between samples were assessed by clustering samples using full rlog transformed count data and multiple ways to calculate distances (Euclidean Distance, Pearson Correlation, Spearman Correlation). Samples generally clustered with other

samples of the same neuronal subtypes, and two major-group structures were observed regardless of the methods used (data not shown) (related to Figure 3.1.1). This also held true with performing analysis using kmeans clustering with a k value of 8 (data not shown). Differential expression tests were performed for every pair of neuronal subtypes, also using the DESeq2 package. Differentially expressed genes (DEGs) were defined using the criteria of a 2-fold change with a false discovery rate (FDR) < 0.01. Subtype uniquely enriched genes (SUEGs) were selected for those that are enriched in the subtype in every pair comparison, thus the FDR criteria for SUEGs after correction for multiple comparisons is ~0.07 (related to Figure 3.1.2 B). Genes whose expression patterns were tested in Figure 3.1.3 were selected from SUEGs, except for Ptgfr, which was found to be enriched in both Aβ SA1-LTMRs and Aβ Field-LTMRs, compared to other subtypes. For the generation of heatmaps shown in Figure 3.1.2, Figure 3.2.1A-B and Figure 4.1.1A, rlog transformed count data was used as expression measurements and as inputs. Genes were first filtered using the criteria of average rlog value across all samples >0, which yielded 18,755 genes, and defined as expressed in Experimental Results sections related to individual figures. For the 18,755 genes detected, rlog averaged across 26 samples for every gene was calculated as average rlog values to represent average expression levels. Average rlog is 14.28 at 99 percentile, 12.59 at 95 percentile, 11.76 at 90 percentile, 10.14 at 75 percentile, 7.74 at 50 percentile and 3.60 at 25 percentile. For the 18,755 genes, rlog differences from the average rlog values were calculated to represent relative expression enrichment or reduction for each sample. A difference of 1 roughly translates to 2-fold change. Rlog differences were then averaged across samples from the same neuronal subtype to represent subtype gene expression differences. Genes were then

grouped based on the neuronal subtype their expression is enriched in, and then ordered based on the enrichment in a descending manner. Only genes that had average rlog values within the top 75% (average rlog > 3.60) and displayed expression differences over 1 in three samples (the number of replicates for one neuronal subtype) were selected for displaying the expression pattern. Rlog difference from the average rlog value was plotted in the main heatmaps using a scale of -2 to 2 represented using blue to red color scale for the heatmaps. Average rlog values were plotted in a second heatmap to the right of the main heatmap. Figure 3.2.2 C-D used the same plotting scheme, but without implementing any filters. Genes were ordered alphabetically. In bar plots displaying gene expression using rpkm values, error bars represent mean ± SD (related to Figure 3.3.1 and Figure 3.3.2A-H). In dotplots diplaying gene expression using rpkm values, all data points were plotted (related to Figure 3.1.3). The bar plots were plotted using Prism 7, while heatmaps and dotplots were plotted using the ggplot2 package in R.

KEY RESOURCES TABLE

REAGENT or RESOURCE	SOURCE/Cat #	IDENTIFIER
Antibodies		
Rabbit anti-GFP (1:1000, IHC)	Invitrogen A11122	AB_221569
Chicken anti-GFP (1:1000, IHC)	Aves GFP 1020	AB_10000240
Rabbit anti-dsRed (1:1000, IHC)	Clontech 632496	AB_10013483
Goat anti-mCherry (1:500, IHC, WM)	Sicgen Ab0040-200	AB_2333092
Rabbit anti-NF200 (1:1000, IHC)	Sigma N4142	AB_477272
Chicken anti-NFH (1:1000, IHC)	Aves NFH0211	AB_2313552
Rabbit anti-TrpC3 (1:300, IHC)	Alomone Labs ACC-016	AB_2040236
Rabbit anti-GABA(A) α1 receptor (1:300, IHC)	Alomone Labs AGA-001	AB_2039862
Rabbit anti-GABA(A) α3 receptor (1:300, IHC)	Alomone Labs AGA-003	AB_2039866
Rabbit anti-Calbindin (1:500, IHC)	Swant CB-38	AB_10000340
Goat anti-TrkC (1:500, IHC)	R&D Systems AF1404	AB_2155412
Goat anti-TrkB (1:500, IHC)	R&D Systems AF1494	AB_2155264
Rabbit anti-CGRP (1:1000, IHC)	Immunostar 24112	AB_572217

Rabbit anti-TH (1:1000, IHC)	Millipore AB152	AB_390204
Sheep anti-TH (1:500, IHC)	Millipore AB1542	AB_90755
Rabbit anti-S100 (1:500, WM)	Dako Z031129-2	AB_2315306
Rabbit anti-Troma1 (1:100, IHC)	DSHB (U of Iowa) TROMA-I	AB_531826
Mouse anti-Kv1.1 (1:250, IHC)	NeuroMab (Antibodies Inc. 75-105)	AB_2128566
Mouse anti-Kv1.2 (1:250, IHC)	NeuroMab (Antibodies Inc. 75-008)	AB_2296313
Mouse anti-Kv1.6 (1:200, IHC)	NeuroMab (Antibodies Inc. 75-012)	AB_2234243
Mouse anti-Kv4.3 (1:250, IHC)	NeuroMab (Antibodies Inc. 75-017)	AB_2131966
Guinea Pig anti-PKCγ (1:1000, IHC)	Frontier Institute Co. Ltd PKCγ-GP-Af350	AB_2571826
IB4-Alexa647 (1:500, IHC)	Invitrogen I32450	N/A
Experimental Models: Organisms/Strains		
Mouse: *MrgD*^{GFP}	Zylka et al., 2005	MGI:3521853
Mouse: CGRP-GFP	GENSAT	MGI:3842528

Mouse: *Th*$^{2A\text{-}CreER}$	Abraira et al., 2017	MGI:5569743
Mouse: *TrkB*^{CreER}	Rutlin et al., 2015	MGI:5616440
Mouse: *TrkB*^{GFP}	Li et al., 2011	MGI:5490140
Mouse: Npy2r-GFP	GENSAT	MGI:3844094
Mouse: *TrkC*^{CreER}	Bai et al., 2015	MGI:97385
Mouse: *Ret*^{fGFP}	Jain et al., 2006	MGI:3691588
Mouse: *PV*$^{ires\text{-}Cre}$	Hippenmeyer et al., 2005	MGI:3590684
Mouse: *R26*$^{LSL\text{-}tdTomato}$ (Ai14)	Jackson Laboratory	JAX:007914 MGI:3809524
Mouse: *Calb1*$^{2A\text{-}dgCre}$	Jackson Laboratory	MGI:5522769
Mouse: *Advillin*^{Flpo}	Bai et al., 2018	N/A
Mouse: *R26*$^{LSL\text{-}FSF\text{-}tdTomato}$ (Ai65)	Jackson Laboratory	JAX:021875
Mouse: *Kcnd3*$^{-/-}$	Jackson Laboratory	MGI:3842528
Mouse: *Brn3a*$^{f(AP)}$	Badea et al., 2012	MGI:3842364
Software and Algorithms		
Clampex 10	Molecular Devices	N/A

Igor	https://www.wavemetrics.com/	
ZEN	ZEISS	SCR_013672
ImageJ/Fiji	Shindelin et al., 2012	SCR_002285
R and RStudio	https://www.r-project.org/ https://www.rstudio.com/	SCR_000432
DESeq2	Love et al., 2014	SCR_015687
ggplot2	Wickham, 2009	SCR_014601
ComplexHeatmap	Gu, et al., 2016	N/A
Prism 7	https://www.graphpad.com/	SCR_005375

*Immunohistochemistry (IHC)

REFERENCES

Abraira, V.E., and Ginty, D.D. (2013). The sensory neurons of touch. Neuron *79*, 618–639.

Abraira, V.E., Kuehn, E.D., Chirila, A.M., Springel, M.W., Toliver, A.A., Zimmerman, A.L., Orefice, L.L., Boyle, K.A., Bai, L., Song, B.J., et al. (2017). The Cellular and Synaptic Architecture of the Mechanosensory Dorsal Horn. Cell *168*, 295–310.e19.

Arcourt, A., Gorham, L., Dhandapani, R., Prato, V., Taberner, F.J., Wende, H., Gangadharan, V., Birchmeier, C., Heppenstall, P.A., and Lechner, S.G. (2017). Touch Receptor-Derived Sensory Information Alleviates Acute Pain Signaling and Fine-Tunes Nociceptive Reflex Coordination. Neuron *93*, 179–193.

Bai, L., Lehnert, B.P., Liu, J., Neubarth, N.L., Dickendesher, T.L., Nwe, P.H., Cassidy, C., Woodbury, C.J., and Ginty, D.D. (2015). Genetic Identification of an Expansive Mechanoreceptor Sensitive to Skin Stroking. Cell *163*, 1783–1795.

Bardoni, R., Tawfik, V.L., Wang, D., François, A., Solorzano, C., Shuster, S.A., Choudhury, P., Betelli, C., Cassidy, C., Smith, K., et al. (2014). Delta opioid receptors presynaptically regulate cutaneous mechanosensory neuron input to the spinal cord dorsal horn. Neuron *81*, 1312–1327.

Barkai, O., Goldstein, R.H., Caspi, Y., Katz, B., Lev, S., and Binshtok, A.M. (2017). The Role of Kv7/M Potassium Channels in Controlling Ectopic Firing in Nociceptors. Front. Mol. Neurosci. *10*, 181.

Basbaum, A.I., Bautista, D.M., Scherrer, G., and Julius, D. (2009). Cellular and Molecular Mechanisms of Pain. Cell *139*, 267–284.

Bocksteins, E., and Snyders, D.J. (2012). Electrically Silent Kv Subunits: Their

Molecular and Functional Characteristics. Physiology *27*, 73–84.

Chawla, K., Tripathi, S., Thommesen, L., Lægreid, A., and Kuiper, M. (2013). TFcheckpoint: a curated compendium of specific DNA-binding RNA polymerase II transcription factors. Bioinformatics *29*, 2519–2520.

Chiu, I.M., Barrett, L.B., Williams, E.K., Strochlic, D.E., Lee, S., Weyer, A.D., Lou, S., Bryman, G.S., Roberson, D.P., Ghasemlou, N., et al. (2014). Transcriptional profiling at whole population and single cell levels reveals somatosensory neuron molecular diversity. Elife *3*, 87.

Coetzee, W.A., Amarillo, Y., Chiu, J., Chow, A., Lau, D., McCormack, T., Moreno, H., Nadal, M.S., Ozaita, A., Pountney, D., et al. (1999). Molecular diversity of K+ channels. Ann. N. Y. Acad. Sci. *868*, 233–285.

Delmas, P., Hao, J., and Rodat-Despoix, L. (2011). Molecular mechanisms of mechanotransduction in mammalian sensory neurons. Nat. Rev. Neurosci. *12*, 139–153.

Dib-Hajj, S.D., Cummins, T.R., Black, J. a, and Waxman, S.G. (2010). Sodium channels in normal and pathological pain. Annu. Rev. Neurosci. *33*, 325–347.

Du, X., and Gamper, N. (2013). Potassium channels in peripheral pain pathways: expression, function and therapeutic potential. Curr. Neuropharmacol. *11*, 621–640.

Du, X., Hao, H., Gigout, S., Huang, D., Yang, Y., Li, L., Wang, C., Sundt, D., Jaffe, D.B., Zhang, H., et al. (2014). Control of somatic membrane potential in nociceptive neurons and its implications for peripheral nociceptive transmission. Pain *155*, 2306–2322.

Everill, B., Rizzo, M.A., and Kocsis, J.D. (1998). Morphologically identified cutaneous afferent DRG neurons express three different potassium currents in varying proportions.

J. Neurophysiol. *79*, 1814–1824.

Fleming, M.S., and Luo, W. (2013). The anatomy, function, and development of mammalian Aβ low-threshold mechanoreceptors. Front. Biol. (Beijing). *8*, 408–420.

Földy, C., Darmanis, S., Aoto, J., Malenka, R.C., Quake, S.R., and Südhof, T.C. (2016). Single-cell RNAseq reveals cell adhesion molecule profiles in electrophysiologically defined neurons. Proc. Natl. Acad. Sci. U. S. A. *113*, E5222-31.

François, A., Schüetter, N., Laffray, S., Sanguesa, J., Pizzoccaro, A., Dubel, S., Mantilleri, A., Nargeot, J., Noël, J., Wood, J.N., et al. (2015). The Low-Threshold Calcium Channel Cav3.2 Determines Low-Threshold Mechanoreceptor Function. Cell Rep. *10*, 370–382.

Gemes, G., Koopmeiners, A., Rigaud, M., Lirk, P., Sapunar, D., Bangaru, M.L., Vilceanu, D., Garrison, S.R., Ljubkovic, M., Mueller, S.J., et al. (2013). Failure of action potential propagation in sensory neurons: mechanisms and loss of afferent filtering in C-type units after painful nerve injury. J. Physiol. *591*, 1111–1131.

Gold, M.S., Shuster, M.J., and Levine, J.D. (1996). Characterization of six voltage-gated K+ currents in adult rat sensory neurons. J. Neurophysiol. *75*, 2629–2646.

Goldman, M.S., Golowasch, J., Marder, E., and Abbott, L.F. (2001). Global structure, robustness, and modulation of neuronal models. J. Neurosci. *21*, 5229–5238.

Gorokhova, S., Gaillard, S., Urien, L., Malapert, P., Legha, W., Baronian, G., Desvignes, J.-P., Alonso, S., and Moqrich, A. (2014). Uncoupling of molecular maturation from peripheral target innervation in nociceptors expressing a chimeric TrkA/TrkC receptor. PLoS Genet. *10*, e1004081.

Grigg, P. (1986). Biophysical studies of mechanoreceptors. J. Appl. Physiol. *60*, 1107–

1115.

Gutman, G.A. (2005). International Union of Pharmacology. LIII. Nomenclature and Molecular Relationships of Voltage-Gated Potassium Channels. Pharmacol. Rev. *57*, 473–508.

Han, L., Ma, C., Liu, Q., Weng, H.-J., Cui, Y., Tang, Z., Kim, Y., Nie, H., Qu, L., Patel, K.N., et al. (2013). A subpopulation of nociceptors specifically linked to itch. Nat. Neurosci. *16*, 174–182.

Hao, J., and Delmas, P. (2011). Recording of mechanosensitive currents using piezoelectrically driven mechanostimulator. Nat. Protoc. *6*, 979–990.

Harper, A.A., and Lawson, S.N. (1985). Electrical properties of rat dorsal root ganglion neurones with different peripheral nerve conduction velocities. J. Physiol. *359*, 47–63.

Heidenreich, M., Lechner, S.G., Vardanyan, V., Wetzel, C., Cremers, C.W., De Leenheer, E.M., Aránguez, G., Moreno-Pelayo, M.Á., Jentsch, T.J., and Lewin, G.R. (2012). KCNQ4 K(+) channels tune mechanoreceptors for normal touch sensation in mouse and man. Nat. Neurosci. *15*, 138–145.

Hippenmeyer, S., Vrieseling, E., Sigrist, M., Portmann, T., Laengle, C., Ladle, D.R., and Arber, S. (2005). A developmental switch in the response of DRG neurons to ETS transcription factor signaling. PLoS Biol. *3*, 0878–0890.

Ikeda, R., Cha, M., Ling, J., Jia, Z., Coyle, D., and Gu, J.G. (2014). Merkel cells transduce and encode tactile stimuli to drive aβ-afferent impulses. Cell *157*, 664–675.

Julius, D. (2013). TRP channels and pain. Annu. Rev. Cell Dev. Biol. *29*, 355–384.

Li, C.-L., Li, K.-C., Wu, D., Chen, Y., Luo, H., Zhao, J.-R., Wang, S.-S., Sun, M.-M., Lu, Y.-J., Zhong, Y.-Q., et al. (2016). Somatosensory neuron types identified by high-

coverage single-cell RNA-sequencing and functional heterogeneity. Cell Res. *26*, 83–102.

Li, L., Rutlin, M., Abraira, V.E., Cassidy, C., Kus, L., Gong, S., Jankowski, M.P., Luo, W., Heintz, N., Koerber, H.R., et al. (2011). The functional organization of cutaneous low-threshold mechanosensory neurons. Cell *147*, 1615–1627.

Liu, P.W., and Bean, B.P. (2014). Kv2 channel regulation of action potential repolarization and firing patterns in superior cervical ganglion neurons and hippocampal CA1 pyramidal neurons. J. Neurosci. *34*, 4991–5002.

Liu, P.W., Blair, N.T., and Bean, B.P. (2017). Action Potential Broadening in Capsaicin-Sensitive DRG Neurons from Frequency-Dependent Reduction of Kv3 Current. J. Neurosci. *37*, 9705–9714.

Löken, L.S., Wessberg, J., Morrison, I., McGlone, F., and Olausson, H. (2009). Coding of pleasant touch by unmyelinated afferents in humans. Nat. Neurosci. *12*, 547–548.

Love, M.I., Huber, W., and Anders, S. (2014). Moderated estimation of fold change and dispersion for RNA-seq data with DESeq2. Genome Biol. *15*, 1–21.

Lu, R., Flauaus, C., Kennel, L., Petersen, J., Drees, O., Kallenborn-Gerhardt, W., Ruth, P., Lukowski, R., and Schmidtko, A. (2017). KCa3.1 channels modulate the processing of noxious chemical stimuli in mice. Neuropharmacology *125*, 386–395.

Maffie, J.K., Dvoretskova, E., Bougis, P.E., Martin-Eauclaire, M.-F., and Rudy, B. (2013). Dipeptidyl-peptidase-like-proteins confer high sensitivity to the scorpion toxin AmmTX3 to Kv4-mediated A-type K + channels. J. Physiol. *591*, 2419–2427.

Maksimovic, S., Nakatani, M., Baba, Y., Nelson, A.M., Marshall, K.L., Wellnitz, S. a, Firozi, P., Woo, S.-H., Ranade, S., Patapoutian, A., et al. (2014). Epidermal Merkel cells

are mechanosensory cells that tune mammalian touch receptors. Nature *509*, 617–621.

McCarter, G.C., Reichling, D.B., and Levine, J.D. (1999). Mechanical transduction by rat dorsal root ganglion neurons in vitro. Neurosci. Lett. *273*, 179–182.

Muqeem, T., Ghosh, B., Pinto, V., Lepore, A.C., and Covarrubias, M. (2018). Regulation of Nociceptive Glutamatergic Signaling by Presynaptic Kv3.4 Channels in the Rat Spinal Dorsal Horn. J. Neurosci. *38*, 3729–3740.

Nakatani, M., Maksimovic, S., Baba, Y., and Lumpkin, E.A. (2014). Mechanotransduction in epidermal Merkel cells. Pflugers Arch. Eur. J. Physiol. *467*, 101–108.

Osteen, J.D., Herzig, V., Gilchrist, J., Emrick, J.J., Zhang, C., Wang, X., Castro, J., Garcia-Caraballo, S., Grundy, L., Rychkov, G.Y., et al. (2016). Selective spider toxins reveal a role for the Nav1.1 channel in mechanical pain. Nature *534*, 494–499.

Pathak, D., Guan, D., and Foehring, R.C. (2016). Roles of specific Kv channel types in repolarization of the action potential in genetically identified subclasses of pyramidal neurons in mouse neocortex. J. Neurophysiol. *115*, 2317–2329.

Patil, M.J., Hovhannisyan, A.H., and Akopian, A.N. (2018). Characteristics of sensory neuronal groups in CGRP-cre-ER reporter mice: Comparison to Nav1.8-cre, TRPV1-cre and TRPV1-GFP mouse lines. PLoS One *13*, e0198601.

Paul, A., Crow, M., Raudales, R., He, M., Gillis, J., and Huang, Z.J. (2017). Transcriptional Architecture of Synaptic Communication Delineates GABAergic Neuron Identity. Cell *171*, 522–539.e20.

Petruska, J.C., Napaporn, J., Johnson, R.D., Gu, J.G., and Cooper, B.Y. (2000). Subclassified acutely dissociated cells of rat DRG: histochemistry and patterns of

capsaicin-, proton-, and ATP-activated currents. J. Neurophysiol. *84*, 2365–2379.

Ranade, S.S., Syeda, R., and Patapoutian, A. (2015). Mechanically Activated Ion Channels. Neuron *87*, 1162–1179.

Rau, K.K., Petruska, J.C., Cooper, B.Y., and Johnson, R.D. (2014). Distinct subclassification of DRG neurons innervating the distal colon and glans penis/distal urethra based on the electrophysiological current signature. J. Neurophysiol. *112*, 1392–1408.

Ritter, D.M., Ho, C., O'Leary, M.E., and Covarrubias, M. (2012). Modulation of Kv3.4 channel N-type inactivation by protein kinase C shapes the action potential in dorsal root ganglion neurons. J. Physiol. *590*, 145–161.

Ritter, D.M., Zemel, B.M., Hala, T.J., O'Leary, M.E., Lepore, A.C., and Covarrubias, M. (2015). Dysregulation of Kv3.4 channels in dorsal root ganglia following spinal cord injury. J. Neurosci. *35*, 1260–1273.

Rudomin, P. (1999). Presynaptic selection of afferent inflow in the spinal cord. J. Physiol. *93*, 329–347.

Rutlin, M., Ho, C.-Y., Abraira, V.E., Cassidy, C., Bai, L., Woodbury, C.J., and Ginty, D.D. (2014). The Cellular and Molecular Basis of Direction Selectivity of Aδ-LTMRs. Cell *159*, 1640–1651.

Sando, R., Baumgaertel, K., Pieraut, S., Torabi-Rander, N., Wandless, T.J., Mayford, M., and Maximov, A. (2013). Inducible control of gene expression with destabilized Cre. Nat. Methods *10*, 1085–1091.

Südhof, T.C. (2012). The presynaptic active zone. Neuron *75*, 11–25.

Sundt, D., Gamper, N., and Jaffe, D.B. (2015). Spike propagation through the dorsal root

ganglia in an unmyelinated sensory neuron: a modeling study. J. Neurophysiol. *114*, 3140–3153.

Trimmer, J.S. (2015). Subcellular localization of K+ channels in mammalian brain neurons: remarkable precision in the midst of extraordinary complexity. Neuron *85*, 238–256.

Tsantoulas, C., and McMahon, S.B. (2014). Opening paths to novel analgesics: the role of potassium channels in chronic pain. Trends Neurosci. *37*, 146–158.

Usoskin, D., Furlan, A., Islam, S., Abdo, H., Lönnerberg, P., Lou, D., Hjerling-Leffler, J., Haeggström, J., Kharchenko, O., Kharchenko, P. V., et al. (2015). Unbiased classification of sensory neuron types by large-scale single-cell RNA sequencing. Nat. Neurosci. *18*, 145–153.

Vacher, H., Mohapatra, D.P., and Trimmer, J.S. (2008). Localization and targeting of voltage-dependent ion channels in mammalian central neurons. Physiol. Rev. *88*, 1407–1447.

Vydyanathan, A., Wu, Z.-Z., Chen, S.-R., and Pan, H.-L. (2005). A-type voltage-gated K+ currents influence firing properties of isolectin B4-positive but not isolectin B4-negative primary sensory neurons. J. Neurophysiol. *93*, 3401–3409.

Wang, R., and Lewin, G.R. (2011). The Cav3.2 T-type calcium channel regulates temporal coding in mouse mechanoreceptors. J. Physiol. *589*, 2229–2243.

Waxman, S.G., and Zamponi, G.W. (2014). Regulating excitability of peripheral afferents: emerging ion channel targets. Nat. Neurosci. *17*, 153–163.

Wellnitz, S. a, Lesniak, D.R., Gerling, G.J., and Lumpkin, E.A. (2010). The regularity of sustained firing reveals two populations of slowly adapting touch receptors in mouse

hairy skin. J. Neurophysiol. *103*, 3378–3388.

Willis, W.D.J., and Coggeshall, R.E. (2004). Sensory Mechanisms of the Spinal Cord - Volume 2 - Back Matter. In Sensory Mechanisms of the Spinal Cord, (Boston, MA: Springer US), pp. 2675–2690.

Woo, S.H., Lumpkin, E.A., and Patapoutian, A. (2015). Merkel cells and neurons keep in touch. Trends Cell Biol. *25*, 74–81.

Woolf, C.J., and Ma, Q. (2007). Nociceptors—Noxious Stimulus Detectors. Neuron *55*, 353–364.

Youssef, N.C.M., Reinhart, K., and Sakr, Y. (2008). The pros and cons of multicentre studies. Netherlands J. Crit. Care *12*, 120–122.

Zhang, X.-L., Mok, L.-P., Katz, E.J., and Gold, M.S. (2010). BK Ca currents are enriched in a subpopulation of adult rat cutaneous nociceptive dorsal root ganglion neurons. Eur. J. Neurosci. *31*, 450–462.

Zimmerman, A., Bai, L., and Ginty, D.D. (2014). The gentle touch receptors of mammalian skin. Science (80-.). *346*, 950–954.

Zylka, M.J., Rice, F.L., and Anderson, D.J. (2005). Topographically Distinct Epidermal Nociceptive Circuits Revealed by Axonal Tracers Targeted to Mrgprd. Neuron *45*, 17–25.

Yang Zheng

Department of Neurobiology, Harvard Medical School
210 Longwood Avenue, Armenise 437• Boston, MA 02215
Phone: 857-777-6323 • E-Mail: yang_zheng@hms.harvard.edu; zylittlep@gmail.com
Nov 16th, 2018

Education

The Johns Hopkins School of Medicine, Baltimore, MD **2011-2018**

Ph.D. in Neuroscience

Tsinghua University, Beijing, China **2006-2010**

B.S. in Biological Science

Research Experience

The Johns Hopkins School of Medicine, Baltimore, MD **2011-2013**

***Harvard Medical School, Boston, MA** **2013-present**

Graduate Student, PI: David D. Ginty, Ph.D.

Defining the molecular basis of somatosensory neuron subtype-specific properties (Publication in revision)

- Characterized mechanosensitive currents in each of the eight major neuronal subtypes using in vitro electrophysiology
- Profiled the transcriptome of eight major somatosensory neuron subtypes by genetic labeling and RNA-sequencing
- Carried out sequencing data analysis and visualization using R programming language
- Identified subtype-specifically enriched genes, among which, a subset were verified by double immunostaining or double fluorescent in situ hybridization
- Developed new mouse genetic strategies for labeling somatosensory neuron subtypes
- Identified ion channels that are differentially expressed among sensory neuron subtypes and determined the expression and function of major potassium channels in collaboration with Dr. Pin Liu and Dr. Bruce Bean
- Mentored and managed three undergraduate students from Simmons College and taught them multiple basic wet-lab techniques. One presented her project in lab and finished her thesis research project under my guidance.

Tsinghua University, Beijing, China **2009-2011**

Undergraduate Student (2009-2010); Research Technician (2010-2011), PI: Bai Lu, Ph.D.

- Research on characterization of subcellular localization of pro- and mature BDNF in hippocampal neurons
- Exploration of a potential behavioral paradigm of maternal deprivation

Tsinghua University, Beijing, China **2008-2009**

SRT (Student Research Training) Student, PI: Dr. Guosong Liu

- Investigation of behavioral enhancement by magnesium-L-threonate(MgT) in learning and memory tasks of Alzheimer's mouse model

Professional Activities

CSHL Course on Electrophysiology: Ion Channels & Synaptic Transmission **Cold Spring Harbor, New York 2015**

SGP Symposium 2014 Sensory Transduction **Woods Hole, MA 2014**

Professional Expertise

Laboratory Skills

RNA-sequencing and data analysis, Mouse Genetics, Cell Electrophysiology, Sensory Biology, Cellular and Molecular Biology

Programming

R (Fluent), Matlab (Summer Bootcamp Course)

Language

Chinese (Native); English (Full Professional Proficiency)

Publications

Ling Bai, Anda M. Chirila, **Yang Zheng**, Brendan P. Lehnert, Pann H. Nwe, Sreyan Chowdhury, Anthony Ramadei, and David Ginty. A-fiber mediated mechanical allodynia and its reliance on dorsal column pathway projections (In revision at Neuron).

Yang Zheng, Pin Liu, Ling Bai, James S. Trimmer, Bruce P. Bean and David Ginty. Deep Sequencing of somatosensory neurons reveals molecular determinants of intrinsic physiological properties (In revision at Neuron)

Presentations

Defining the molecular basis of somatosensory neuron subtype-specific properties HMS Department Seminar, 2018

RNA profiling of major DRG sensory neuron subtypes – A resource for indentification of genes involved in mechanosensation. SGP symposium of Sensory Transduction, 2014